The Dissertation Committee for Dmitry Meyerson
certifies that this is the approved version of the following dissertation:

Electostatic Plasma Edge Turbulence and Anomalous Transport in SOL Plasmas

Committee:

Ken Gentle, Supervisor

Francois Waelbroeck, Co-Supervisor

Roger Bengtson

Craig Michoski

Wendell Claude Horton

Philip Morrison

Electostatic Plasma Edge Turbulence and Anomalous Transport in SOL Plasmas

by

Dmitry Meyerson, A.B., M.A.

DISSERTATION

Presented to the Faculty of the Graduate School of

The University of Texas at Austin

in Partial Fulfillment

of the Requirements

for the Degree of

DOCTOR OF PHILOSOPHY

THE UNIVERSITY OF TEXAS AT AUSTIN

August 2014

To the memory of my father, Felix Meerson.

Acknowledgments

I would like to thank Dr. Francois Waelbroeck, who encouraged and supervised my work at the Institute of Fusion Studies (IFS) at UT Austin. In addition to providing consistent feedback and guidance Dr. Waelbroeck secured financial support and academic travel support that made it possible for me to focus on my research during a crucial period of my PhD program as well as engage with the broader research community. His management of IFS in parallel with supervising multiple research projects, while maintaining a positive, energetic attitude inspires me to be a better scientist.

I would like to thank Dr. Craig Michoski who selflessly took time to introduce to me to numerics, was willing to examine every detail of my work, and whose fervor for fusion was renewing every time we interacted. His perspective as a scientist who manages multiple professional and personal responsibilities was invaluable.

Many thanks go to Dr. Wendell Horton and the Horton Turbulent Transport Group (Cynthia Correa, Ehab Hassan, Jingfei Ma, Xianrong Fu, David Gogichaishvili) who provided a ready audience and a sounding board. The group presented a forum in which I could present my work, ask questions, and be challenged to learn something new on a regular basis. Dr. Horton in particular expanded my breadth of knowledge by encouraging me to examine space plasmas. He also provided financial support and encouragement in a period of uncertainty.

I would also like to thank Dr. Ken Gentle, who arranged financial support during

my time as an experimentalist. Dr. Gentle continued to be a reliable adviser and source of experimental insight even after my transition to computational work.

I owe a debt of gratitude to everyone on whom I imposed half-formed questions and unfocused physics discussions, both for tolerating that sort of interaction and for more often than not sending me away with an answer, an insight, or at the very least a clear idea of what needs to be asked next. IFS members Dr. Hatch, Ryan White and Dr. Waelbroeck: Thank you all.

I am grateful to my wonderful wife Jessica whom I met while a graduate student here in Austin. She has become my constant companion and best friend in the last six years. She was always there to earnestly support me with her kindness and honesty.

Finally I want to thank my parents, Felix Meerson and Elena Vorontsova, who by their own example instilled values of lifelong curiosity for its own sake, the joy of learning and teaching, and a healthy skepticism of one's own ideas, habits, knowledge and skills.

Electostatic Plasma Edge Turbulence and Anomalous Transport in SOL Plasmas

Publication No. _____

Dmitry Meyerson, Ph.D.
The University of Texas at Austin, 2014

Supervisors: Ken Gentle
Francois Waelbroeck

Controlling the scrape-off layer (SOL) properties in order to limit divertor erosion and extend component lifetime will be crucial to successful operation of ITER and devices that follow, where intermittent thermal loads on the order of GW/m^2 are expected. Steady state transport in the edge region is generally turbulent with large, order unity, fluctuations and is convection dominated. Owing to the success of the past fifty years of progress in magnetically confining hot plasmas, in this work we examine convective transport phenomena in the SOL that occur in the relatively "slow", drift-ordered fluid limit, most applicable to plasmas near MHD equilibrium. Diamagnetic charge separation in an inhomogeneous magnetic field is the principal energy transfer mechanism powering turbulence and convective transport examined in this work.

Two possibilities are explored for controlling SOL conditions. In chapter 2 we review basic physics underlying the equations used to model interchange turbulence in the SOL and use a subset of equations that includes electron temperature and externally

applied potential bias to examine the possibility of suppressing interchange driven turbulence in the Texas Helimak. Simulated scans in $\mathbf{E_0} \times \mathbf{B_0}$ flow shear, driven by changes in the potential bias on the endplates appears to alter turbulence levels as measured by the mean amplitude of fluctuations. In broad agreement with experiment negative biasing generally decreases the fluctuation amplitude. Interaction between flow shear and interchange instability appears to be important, with the interchange rate forming a natural pivot point for observed shear rates.

In chapter 3 we examine the possibility of resonant magnetic perturbations (RMPs) or more generally magnetic field-line chaos to decrease the maximum particle flux incident on the divertor. Naturally occurring error fields as well as RMPs applied for stability control are known to cause magnetic field-line chaos in the SOL region of tokamaks. In chapter 3 2D simulations are used to investigate the effect of the field-line chaos on the SOL and in particular on its width and peak particle flux. The chaos enters the SOL dynamics through the connection length, which is evaluated using a Poincaré map. The variation of experimentally relevant quantities, such as the SOL gradient length scale and the intermittency of the particle flux in the SOL, is described as a function of the strength of the magnetic perturbation. It is found that the effect of the chaos is to broaden the profile of the sheath-loss coefficient, which is proportional to the inverse connection length. That is, the SOL transport in a chaotic field is equivalent to that in a model where the sheath-loss coefficient is replaced by its average over the unperturbed flux surfaces. Both fully chaotic and the flux-surface averaged approximation of RMP application significantly lower maximum parallel particle flux incident on the divertor.

Table of Contents

[1]This chapter is based on previously published work [52]. The author acknowledges multiple revisions and discussions with Dr. Francois Waelbroeck and Dr. Craig Michoski. The author is grateful to Dr. Wendell Horton's insightful feedback.

List of Tables

List of Figures

Chapter 1

Introduction

The initial construction phase of the International Thermonuclear Experimental Reactor (ITER) is expected to be complete in 2020. While there is great optimism in achieving high fusion energy gain factors, with $Q \geq 10$ expected, concerns regarding large intermittent thermal loads as well impurity contamination must be addressed. The expected steady state heat flux on ITER's divetor plates is expected to be up to 20 MW/m^2 on the divertor plates and about .5 MW/m^2 on the first wall [51, 40], and larger still in reactors that follow. In addition to steady state loads, high thermal loads (on the order of GW/m2) due to edge localized modes (ELMs) and disruptions, lasting on the order of (1ms - 10ms) may cause unacceptable plasma facing component (PFCs) erosion, shorten material lifetimes and challenge the capacity of the actively cooled heatsinks situated immediately behind the PFCs. A partial solution to the excessive heat flux problem is to use higher Z value PFC materials with superior thermo-mechanical properties, tungsten being the prime example. However the steady state transport in the edge region is generally turbulent with large, order unity, fluctuations and readily forming, coherent, field-aligned, convective transport structures facilitating inward transport of impurities and outward transport of particles and heat. While partially addressing previously raised concerns, the use of higher Z materials may exacerbate radiative cooling due to higher Z impurity transport.

The principal goal of modern fusion research is to understand how externally applied sources of particles, momentum, energy or appropriate rearrangements of magnetic geometry can reduce overall transport and lengthen intervals free of violent bifurcations such as ELMs or sawtooth disruptions [43, 82]. In this work we choose to consider two externally applicable control mechanisms. Specifically in section we turn attention to the Texas Helimak plasma device in section 2, we consider how externally applied potential and the resulting changes in the equilibrium $\mathbf{E_0} \times \mathbf{B_0}$ convection and more importantly velocity shear may suppress, enhance or otherwise alters interchange driven density fluctuations[86]. Discussion of tailoring an appropriate 2D two-fluid model is presented in section 2.2. In section 3 we consider how augmenting the classical symmetric toroidal field with an external set of antenna coils (RMPs) rearranges the magnetic geometry and in turn changes profile of quasi-steady-state SOL plasmas.

The literature uses the term 'anomalous transport' to describe transport mechanisms that enable transport in excess of simple diffusion. This label is something of a misnomer, as it is in fact the norm rather than the exception. In the best, but experimentally unfounded scenario, in the far scrape-off-layer (SOL) fast parallel transports dominates the relatively weak cross-field Bohm diffusion, resulting in relatively short e-folding lengths in the scrape-off layer (SOL) facing the main chamber wall. However experimentally observed large SOL widths [73], direct observation of convected coherent structures, and order unity density fluctuations in the edge region are consistent with anomalous transport. Typically two major types of coherent object are associated with enhanced transport in the region beyond the last closed flux surface(LCFS), edge localized modes and blobs that are smaller, generally amenable to electrostatic treatment, and less

disruptive.

1.1 Tokamaks and the scrape-off layer

Two major complementary pathways to predicting and understanding how a fusion device behaves are available; experimental scans along dimensionless parameters [59, 50] and theoretical modeling that often involves extensive numerical work. The focus of this dissertation is the edge region where a large set of instabilities and practical complications can negatively impact core plasma conditions, possibly keeping ITER and other next-generation devices from reaching predicted fusion power conditions. The edge region is thus uniquely important in fusion because of the need to sustainably absorb outgoing thermal and particle fluxes, control plasma recycling at both divertor and main chamber wall surfaces, and enable conditions that minimize anomalous transport. Each objective is difficult to treat in isolation from the others. Here we concentrate on the convective transport phenomena in the edge region of magnetic confinement machines.

Not unlike simpler system that can often be formulated as boundary value problems, where the boundary conditions completely determine the interior solution, the core region in fusion plasma devices is very sensitive to the edge region conditions. Extending this analogy further, the edge region is in fact a turbulent dynamic boundary condition. Changes in the SOL turbulence character, flow and flow shear, and magnetic geometry in turn influence the set of allowed eigenmodes in the core region, which in turn modifies the transport and then the plasma profiles in the core. Thus we see that there is a two way coupling of the edge and plasma profiles. The core and edge regions are usually treated separately, due to very different collisionalities, consequently the dominant

transport channels and instabilities differ in the two regions. Collisionality influences the appropriate closure scheme in a fluid description or in the extreme case of very low collisionaity precludes a fluid closure altogether, demanding a kinetic treatment. From a modeling stand point core turbulence and transport will typically demand the use of gyro-kinetic codes, while the edge region where plasmas are more collisional can be modeled with an appropriate subset of the traditional two-fluid Braginskii equations. Additionally a more complex geometry found in the edge regions further encourages the use of edge-specific codes well suited to the non-trivial geometry.

The edge plasma outside the separatrix operates in a regime where parallel transport greatly exceeds cross-field transport simply due the nature of magnetic confinement where $\frac{\rho}{L} << 1$, where ρ is the Larmor radius and L is macroscopic length scale descriptive of the system. The field lines terminate on the divertor plates designed with high thermal fluxes in mind. In the best case scenario perpendicular transport provides an additional, well controlled, diffusive channel that lessens the thermal and particle loads on the divertor plates. However, the reality is that the edge regions in fusion devices universally exhibit plasma turbulence, zonal flows, and violent edge localized modes (ELMs) all resulting in large variances in heat and particle flux on the plasma facing components and a scrape-off layer width that greatly exceed predictions based on purely diffusive transport. Should excessive heat or particle flux impact on the vessel walls the resulting introduction of impurities to the core will greatly enhance radiative cooling - moving the plasma conditions away from a self-sustaining exothermic state.

The task of minimizing intermittent cross-field transport is complicated by the presence of a fast convective transport channel facilitated by cohesive self-propagating

structures commonly called 'blobs', in reference to their shape and their order unity aspect ratio in the plane normal to the magnetic field-lines. While blobs travel radially outward, closely related 'holes' or localized depletions travel inward and will readily facilitate impurity transport into the core region. Even if the edge region is sufficiently wide and blob velocity is sufficiently slow such that the vessel walls are only minimally impacted just the localized nature of these structures typically implies a corresponding localized heat and particle deposition footprint on the divertor plates [25]. While the divertor plates are built with maximum tolerable heat and particle flux in mind, nonetheless highly localized heat flux loads can result in excessive erosion, material sputtering, and sub-optimal device operation.

Parameter	Value
collision frequency	$\nu_{ei} \approx 1 \times 10^2 Hz - 1 \times 10^5 Hz$
major radius	$R_0 \approx 50cm - 150cm$
parallel connection length	$L_{\|} \approx 2\pi q R_0 \approx 300cm - 1 \times 10^3 cm$
electron temperature	$T_e = 1eV - 1000eV$
electron density	$n_e \approx 1 \times 10^{11} cm^{-3} - 1 \times 10^{13} cm^{-3}$
ion temperature	$T_i \approx 1eV - 10eV$
ion-acoustic gyroradius	$\rho_s \approx .1cm - 2cm$
ion-acoustic gyro frequency	$\omega_{ci} \approx 5 \times 10^7 - 5 \times 10^8$

Table 1.1: Typical SOL parameters[81]

1.2 fluid models

Lorentz force together with Maxwell equations gives us a complete description of the plasma motions. This physical description generally lives in a 6-N, with N being the total number of particles in the system, dimensional phase (q, p) space. Keeping track

of the position and velocity of each particle in phase phase is not practical nor can this information be immediately understood in terms of experimental observables. The most common approach is to reformulate the Maxwell-Lorentz equations in terms of one-body particle distributions $f_\alpha\left(x, p, t\right)$ in phase space, where α denotes the type of particle - ion, electron or impurity ions. The assumptions and mathematical machinery underlying this approach are well reviewed in Hazeltine and Meiss [35]. Specifically fluid theory only keeps a few leading moments of the particle distribution in velocity space and generates models in terms of several fluid variables in two or three dimensional coordinate space. As pointed out by [35], this has the advantage of working with variables that are directly observed in experiments.

Fluid theories describe plasma motion in terms of a hierarchy of coupled moments of the ensemble averaged distribution function $f_s(r, v, t)$, where the lowest order moments have names and a clear physical interpretation associated with them, density, flow velocity, pressure and a few others [35, 36, 41]. The moments of the kinetic equation provide equations that describe the evolution of any given moment in coordinate space, in terms of itself, lower moments, as well as higher order moments. Letting M_k represent the k_{th} moment of the particle distribution in velocity space, then k_{th} of the Vlasov equation will couple M_k to a set of moments,

$$M_k = F\left[M_0, ...M_k, M_{k+1}\right]. \tag{1.1}$$

Unless additional assumptions are made, the evolution of any given moment will depend on higher order moments. To truncate the system at some finite number of

equations we have to close it by expressing higher moments in terms of lower order moments. A description of asymptotic closure of plasma fluid equations for collisional plasmas, where the small ratio of the mean-free-path to some characteristic macroscopic length-scale is the used as the basis of asymptotic expansion, was first presented by S.I.Braginkskii in 1967 [11]. For example, the single fluid MHD description truncates the simple description at $M_{k=3}$ and reduces $M_{k=2}$ by assuming the off diagonal term of $M_{k=2}$ terms are negligible. Excluding the possibilities offered by more exotic closure schemes [38, 13], the typical closed system of fluid plasma equations is most applicable in collisional regimes, such as the scrape-off layer (SOL) of magnetically confined machines. As such, we limit our attention to regimes where background length scales are much longer than the ion Larmor radius and timescales are longer than the typical inverse gyro-frequencies. Fluid models depend on kinetic assumptions for closure, typically an assumption of a shifted Maxwellian distribution in velocity space with small FLR correction term. Fluid closure schemes that can reproduce parallel Landau damping and some other kinetic effects can be used [70].

In terms of both physical fidelity and numerical complexity fluid-based modeling is often a compromise between more empirically oriented 1D and $1\frac{1}{2}$D transport codes [60] and more complex, and physically complete, gyro-kinetic codes such as GYRO and GS2 [12, 19]. Drift ordered fluid models in particular are well suited to describing plasma phenomena that are slow compared to typical thermal velocities V_{th} and provide a simple, if not totally systematic, but reasonably accurate description of plasma fluctuations and instabilities near MHD equilibrium [35, 26]. Unlike cold-plasma and MHD limits, where pressures driven drifts are neglected or are very small compared to $\mathbf{E} \times \mathbf{B}$ drifts,

fluid equations in the drift limit retain ion and electron pressure driven magnetic drifts that are on the same order as $\mathbf{E} \times \mathbf{B}$ drifts. Diamagnetic charge separation is the principal energy transfer mechanism powering turbulence and convective transport examined in this work. In seeking to equilibrate radial inhomogeneities of a typical SOL magnetic field diagmagnetic currents will polarize localized pressure homogeneities and drive them radially outward with respect to the prevailing magnetic curvature.

Chapter 2

Sheath connected blobs in the Texas Helimak

2.1 The Texas Helimak

The Texas Helimak is designed to investigate basic SOL physics without the geometric complications that are specific to tokamak SOL regions. In particular in a toroidal system a given blob, while highly localized in the plane normal to the field line may in fact be greatly extended along the field line such that the radius of curvature varies accordingly. As pointed out by D.D. Ryutov [68] estimating the effect of net curvature-induced polarization and subsequent cross field motion requires a nontrivial averaging procedure and an inclusion of sufficiently large viscous forces to allow a blob-filament to move as a single unit through the SOL even as different segments experience differing effective gravity. In the Helimak the major radius associated with a given field does not vary, making the average radius of curvature trivial to compute and uniform along the field line. The geometry is well suited to verifying results obtained from models in the slab approximation, while retaining shear and curvature effects found in tokamak SOL regions.

The device combines sixteen toroidal field coils with three vertical field coils. The toroidal field dominates the magnetic geometry with a magnetic field that is at least 10 times greater than the vertical, effective poloidal, field at roughly .1 Tesla. In general the

resulting set of nested helical surfaces are characterized by very long connection lengths, up to several kilometers. Four groups of four (two on top and bottom, 180 degrees apart) toroidally facing bias plates covering the radial extents of the vacuum chamber allow for the addition of externally applied bias to the natural sheath potential. This external biasing can in turn change the equilibrium $\mathbf{E} \times \mathbf{B}$ vertical flow velocities present in the plasma.

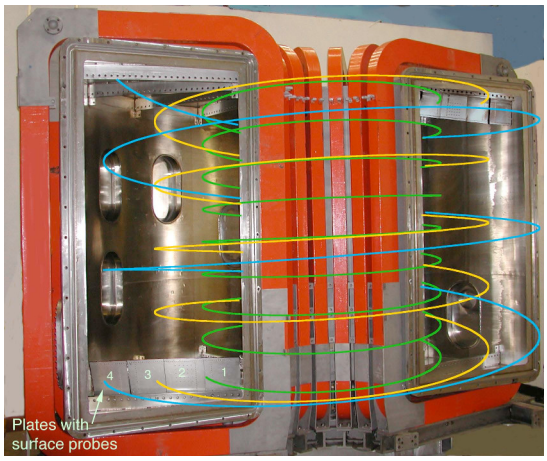

(a) The Helimak is an experimental realization of a sheared slab scrape-off layer with curvature drive. The pictured endplates allow for biasing the potential as well proving a platform for diagnostics.

(b) The toroidal coil (in red) provides the dominant field and allows for kilometer long connections lengths in an otherwise practically sized device. The much smaller vertical field is generated by three vertical field coils (blue coils).

Figure 2.1: Helimak

Shear suppression of turbulence in both plasmas and neutral fluids [74] is intuitively straightforward to understand. A coherent object such as a blob once stretched

to several times it's coherence length will rapidly breakup as it interacts with its similar deformed neighbors, shortening the spatial correlation length in the shear-wise (radial) direction. The new smaller structures will be elongated along the flow direction. For the particular case of blobs, that depend on co-located potential structures to be convected radially outward, this may further reduce convective radial flux. As illustrated in figure (3.1), the potential dipole is driven by electron pressure inhomogeneity along the bi-normal direction, which in the presence strong flow shear may itself be reduced. Plasma devices conditioned to operate with long intervals of steady-state flow shear and associated transport barriers are largely responsible for improved confinement for the last two decades [74]. The Texas Helimak is a unique platform to test shear facilitated turbulence suppression, with a simple one-dimensional equilibrium, straightforward means of influencing the mean ϕ profile via external biasing, detailed diagnostics, and SOL-like physics.

The pitch angles are typically small enough for all field lines to terminate on the bias plates. In addition to shifting the sheath potential the plates are a convenient platform to mount an array of Langmuir probes[32].

2.2 model equations

To put the equations used in modeling a Helimak-like system in context a quick review of the fundamentals and discussion of specific terms are useful. A number of great references exist that follow up on Braginskii's original work [11], and derive equations specifically geared to SOL simulations [21, 78]. In building our model we seek to start with a relatively general subset of fluid equations that are applicable to low-β, small $\frac{T_i}{T_e}$,

Parameter	Value
collision frequency	$\nu_{ei} \approx 1 \times 10^5 Hz$
major radius	$\langle R_0 \rangle = 1.1cm$
parallel connection length	$L_{\parallel} \approx 1 \times 10^4 cm - 3 \times 10^6 cm$
electron temperature	$T_e = 10eV$
electron density	$n_e <= 1 \times 10^{11} cm^{-3}$
ion temperature	$T_i \approx .1eV$
ion-acoustic gyro-radius	$\rho_s \approx 2cm$
ion-acoustic gyro-frequency	$\omega_{ci} \approx 2 \times 10^5 \frac{rad}{s}$
c_s	$5 \times \times 10^3 \frac{cm}{s}$
B field toroidal	$B_T \approx .1T$
B field poloidal	$B_P \leq .01T$
Collisionality	$\frac{\lambda_{ee}}{L_{\parallel}} \approx 40$

Table 2.1: Typical Helimak parameters(Argon gas) [32],[58]

SOL plasmas with characteristic frequencies much slower that ion-gyro frequencies for either ion or electrons.

$$\partial_t \approx \frac{1}{\tau} \approx \left(\frac{\rho_s}{L}\right)^2 \omega_{ci} << \omega_{ci} \tag{2.1}$$

To model interchange turbulence in the Helimak we concentrate on a subset of Braginskii equations with cold ions, which significantly simplifies the equations [86] by removing P_i equation as well as additional terms in the remains. This approximation often stays close to experimentally relevant regimes for edge plasmas, where $T_i < T_e$ is a common condition due to the heating schemes and mass difference. In particular, in the Helimak the plasma is generated by applying electron cyclotron heating on a neutral argon or helium gas, and as mentioned in more detail in section 2.5 this heating scheme preferentially heats electrons. The slow thermalization time between electrons and ions

assures the the cold ion limit is valid. In the Helimak the relative ion temperature remains very cold, with $\frac{T_i}{T_e} \approx= .1 - .01$. Still situations where $T_i \approx T_e$ happen frequently enough and finite ion temperature effects on SOL transport have been included in detailed SOL studies [84]. In the cold-ion, electrostatic limit prior to normalizing or averaging along magnetic field lines, our basic equations are continuity, charge conservation, electron temperature as well parallel ion velocity. We obtain parallel current and velocities in the limit of massless electrons from parallel electron momentum balance, or in the case of open fields from elementary sheath theory where electrons and ions have to be considered separately.

The relative amplitude of fluctuations in the SOL is often comparable to the mean value of the field in question, specifically for the Helimak the density fluctuations are observed to $\frac{\Delta n}{n} \approx .4$. Rather than drive our system with some predetermined gradient we instead have a flux driven system where both the mean gradient and the fluctuations are set by the physics of the system in addition to the source term [69]. Barring a more complex model where the fluctuating and mean part of a given field are evolved separately and are coupled in a self-consistent way, simply evolving the entire profile is a justified approach for the Helimak and similar SOL systems.

2.2.1 continuity

We can start with a relatively general continuity expression that includes $\mathbf{E} \times \mathbf{B}$ convection, curvature drive, parallel losses, diffusive terms as well external sources and sinks. In the drift-ordered limit, discussed in section 1, we are free to evolve either an ion or an electron fluid, to avoid including the somewhat cumbersome ion polarization drift

we evolve the electron number density.

$$\partial_t n + V_E \cdot \nabla n = \frac{2}{B}\hat{b} \times \hat{\kappa} \cdot (\nabla P_e - n\nabla\phi) - \nabla_{\parallel}\left(nV_{e,\parallel}\right) + D_n\nabla^2 n + S_n \tag{2.2}$$

2.2.2 charge conservation or vorticity

Demanding a locally quasineutral plasma we conclude that divergence of the current must vanish everywhere,

$$\partial_t n_e = \partial_t n_i \rightarrow \nabla\left(n\left(V_i - ZV_e\right)\right) = 0. \tag{2.3}$$

In equation 2.3 Z is the ionization state of the ions and the fluid velocities are composed of lowest order perpendicular drifts , as well as parallel velocities and the ion polarization drift. The quasi-neutrality constraint, simplified using the Boussinesq approximation [1], can be rewritten in terms of dynamic $V_{E\times B}$ flow vorticity, or equivalently $\nabla^2_{\perp}\phi$. For convenience we define $\varpi \equiv \nabla^2_{\perp}\phi$.

As illustrated in figure (3.1), the boxed curvature term in the vorticity equation

$$\partial_t \varpi + \left(V_E + V_{i,\parallel}\hat{b}\right) \cdot \nabla\varpi = \boxed{2\frac{B\hat{b} \times \hat{\kappa} \cdot \nabla P_e}{n}} + \frac{B^2}{n}\nabla_{\parallel} j_{\parallel} + D_{\varpi}\nabla^2\varpi, \tag{2.4}$$

is key to polarizing local density maxima and enabling fast convective transport in regions with unfavorable curvature. Many SOL blob studies neglect the curvature terms in the density and temperature equations, as the basic blob generation does not require those particular terms, however curvature terms are physical in all three equations and

[1] motivated by mostly mathematical convenience this approximation unfortunately assumes small density fluctuations, $\frac{\Delta n}{n} << 1$, which is definitely not true for flux driven systems considered in this work

from basic linear analysis can be shown to be stabilizing at larger wavelengths. In a numerical context this is a helpful feature which stabilizes fluid models without introducing un-physical, ad-hoc diffusion. Perhaps the principal justification for this common approximation is that for many cases $\frac{L_{n,T}}{R_0} << 1$ resulting in diamagnetic drifts that dwarf curvature drifts.

While a blob may still form and convect with $E \times B$ velocty in the absence of a curvature drive, without curvature drive to create a co-located dipole potential structure the density maxima cannot propagate as quickly and will interact with existing turbulence found in the plasma and be at the mercy of random correlation of fluctuations, rather than "bring its own" radially bound coherent transport structure.

2.2.3 electron temperature, energy

If we wish to address heat flux in addition to density flux an electron pressure or a temperature equation is required.

$$\partial_t T_e + \left(V_E + V_{e,\|}\hat{b}\right) \cdot \nabla T_e = \frac{4}{3}\frac{T_e}{Bn}\hat{b} \times \hat{\kappa} \cdot \left(\nabla P_e - n\nabla\phi + \frac{5}{2}n\nabla T_e\right) + \frac{2T_e}{3n_i}\left(\beta\nabla_{\|} j_{\|} - n\nabla_{\|} V_{e,\|}\right) + S_{T_e} \tag{2.5}$$

2.2.4 simplified geometry

For devices where the major radius of curvature R varies weakly along the field line, or studies where we chose to focus on regions described by such magnetic geometry locally, we can do away with much of the vector notation in eqs. (2.2), (2.4) and (2.5).

expanding around $\frac{B_P}{B_T} << 1$ we can show that

$$\hat{\kappa} \approx -\frac{1}{R}\left(1 - \mathcal{O}\left(\frac{B_P}{B_T}\right)^2\right)\hat{e}_r, \tag{2.6}$$

$$\hat{b} \times \hat{\kappa} \cdot \nabla F = \frac{1}{R}\frac{Cos\,(\theta)}{r}\partial_\theta F + \mathcal{O}\left(\frac{B_P}{B_T}\right), \tag{2.7}$$

where θ is a displacement along the poloidal projection of a field line as it travels over a flux surface. Note that the curvature drive flips sign when the field moves between to the high B field side of the torus, with the radially outward directed curvature drive defining the region of destabilizing, commonly named bad curvature.

In SOL models, we frequently define some effective gravity coefficient g where

$$g = \frac{2}{R} = -2\kappa_r \tag{2.8}$$

As pointed out above the effective gravity due to curvature drift can vary greatly as we move along a field line. However for geometries where the major radius is uniform along a field line and $\frac{B_P}{B_T} << 1$ such is the at the Texas Helimak, or when we limit the scope of a given study to the outer midplane, we can greatly simplify the vector notation in eqs. (2.2), (2.4) and (2.5).

$$\hat{b} \times \hat{\kappa} \cdot \nabla\,(\,\ldots\,) \rightarrow \frac{g}{2}\partial_y\,(\,\ldots\,) \tag{2.9}$$

2.2.5 $J_{\parallel}$ closure

In the electrostatic limit we can find the parallel current from the parallel component of the electron momentum equation, this is simply Ohm's law for our context.

$$\cancelto{\approx 0}{m_e n_e \frac{dv_e}{dt}} = -\nabla p_e - e n_e \left[E + \frac{v_e}{c} \times B \right] + R_{ei} \tag{2.10}$$

Calculating perpendicular electron velocities consistent with electron momentum balance yields the usual $v_{E\times B}, v_{de}$ drifts. Parallel momentum balance will allow us to to close our equations. The collisional force is

$$R_{ei} = (ne\frac{j_{\parallel}}{\sigma_{\parallel}} - \beta n \nabla_{\parallel} T_e) \tag{2.11}$$

where the parallel conductivity is set by the collisionality of the plasma
$\sigma_{\parallel} = \frac{2ne^2}{\nu_{ei} m_e}$ with $\nu_{ei} \approx \frac{Z_{eff} n e^4 \lambda}{4\pi\epsilon_0 \sqrt{m_e} T_e^{\frac{3}{2}}}$

putting it all together yields $j_{\parallel}$

$$j_{\parallel} = \sigma_{\parallel} \left(\frac{\nabla_{\parallel} p_e}{en} - \nabla_{\parallel}\phi + \frac{\beta}{e}\nabla_{\parallel} T_e \right)$$

with a little bit of algebra we can rewrite $j_{\parallel}$ in terms of normalized quantities

$$j_{\parallel} = \underbrace{(en_0 v_{th,e})}_{j_0} \cancelto{\tilde{\sigma}_{\parallel}}{\left(2 \underbrace{\frac{m_i}{m_e}}_{\mu} \underbrace{\tau_{ei}\omega_{ci}}_{\tilde{\tau}} \right)} \tilde{T}_e^{\frac{3}{2}} \left(\tilde{\nabla}_{\parallel} \log[\tilde{n}] - \tilde{\nabla}_{\parallel}\tilde{\phi} + (\beta + 1)\tilde{\nabla}_{\parallel}\tilde{T}_e \right) \tag{2.12}$$

dropping˜superscript the re-scaled parallel current when quasineutrallity is satisfied will appear as:

$$j_{\parallel} = \sigma_{\parallel} T_e^{\frac{3}{2}} \left(\nabla_{\parallel} \log[n] - \nabla_{\parallel} \phi + (\beta + 1) \nabla_{\parallel} T_e \right) \tag{2.13}$$

In simulations where 3D geometry is implemented or 2D simuluations where a particular parallel mode is fixed [58], the preceding description of $j_{\parallel}$ is appropriate, however as we reduce the dimensionality of our system by averaging along the field lines the closure scheme must somehow express $\nabla_{\parallel} j_{\parallel}$ in the plane normal to the field-line.

2.2.6 sheath boundary conditions - sheath connected limit

In the far SOL we can consider blobs in the sheath connected limit, and use parallel current predicted by basic sheath theory as a boundary condition or equivalently a closure method to eliminate $\nabla_{\parallel} j_{\parallel}$ from our equations. Near the sheath our plasma is no longer quasineutral, so we have to treat electrons and ions separately. Taking cold ions $n_i = n \left[1 - \frac{2e}{m_i V_{th}^2} (\phi - \phi_w) \right]^{-\frac{1}{2}}$

and Boltzmann electrons $n_e = n e^{\frac{e(\phi - \phi_w)}{T_e}}$,

we can show that

$$j_{\parallel, sheath} = en \sqrt{\frac{T}{m_i}} \left[1 - \left(\frac{m_i}{2\pi m_e} \right)^{\frac{1}{2}} e^{\frac{e(\phi_s - \phi)}{T_e}} \right] \tag{2.14}$$

.

We define ϕ_s, the plasma potential on the sheath edge, by considering the steady condition $j_{\parallel} = 0$ at the sheath edge, and define a convenient sheath parameter Λ.

$$\frac{e(\phi_s)}{T_e} = ln\left(\frac{m_i}{2\pi m_e}\right)^{\frac{1}{2}} = \Lambda$$

It follows that in general the potential profile can related to the equilibrium temperature profile $T_e(x)$, and wall bias $\phi_w(x)$.

$$\phi_s(x) = \frac{\Lambda T_e(x)}{e} - \phi_w(x), \tag{2.15}$$

where $\phi_w(x)$ is the potential on the conducting wall, this is where any externally applied wall bias would enter the physics.

Near the field-line ends current and parallel electron velocity are then shown to be:

$$j_{\parallel,sheath} = j_0\left[1 - e^{\Lambda - \frac{e\phi}{T_e}}\right] \tag{2.16a}$$

$$V_{\parallel,e} = V_{th}\left[e^{\Lambda - \frac{e\phi}{T_e}}\right] \tag{2.16b}$$

.

often small $\frac{e\phi}{T_e}$ deviations from the sheath parameter are assumed and only the fluctuating component is taken into account.

$$j_{\parallel,sheath} \approx j_0 \frac{e\phi}{T_{e0}}$$
$$V_{\parallel,e} \approx V_{th}\left[1 - \frac{e\phi}{T_{e0}}\right]$$

In normalized form, with a uniform temperature, the field line average of $\nabla \cdot j_{\parallel}$ and $\nabla \cdot V_{\parallel,e}$ reduces to simpler expressions commonly seen in interchange models. To illustrate, consider an average along the field, being careful to recognize that expression

2.16 refers to current directed towards the divertor, so the direction changes sign when we go from one end of the field line to another, yielding a factor of two in the definition of α as it appears in equation (2.17).

$$\langle \nabla_{\parallel} j_{\parallel} \rangle_{\parallel} \Rightarrow \underbrace{\frac{2\rho}{L_{\parallel}}}_{\alpha} n \left(1 - e^{\Lambda - \phi}\right) \approx \alpha \, n \, \delta\phi \tag{2.17a}$$

$$\langle n \nabla_{\parallel} v_{\parallel,e} \rangle_{\parallel} \Rightarrow \alpha \, n \, e^{\Lambda - \phi} \approx \alpha \, n \, (1 - \delta\phi) \tag{2.17b}$$

Several other closure schemes for $J_{\parallel}$ that facilitate 2D representation exists, including schemes appropriate in the vicinity of the X-point, purely dissipative closure, electromagnetic closure, and others described clearly by Krasheninnkov *et al.* (2008) [43].

2.2.6.1 Field line averaging

Not all terms in eqs. (2.2), (2.4) and (2.5) can easily be averaged along the field line without assuming some parallel mode structure.

$$\frac{1}{L_{\parallel}} \int_{sheath} \nabla_{\parallel} F = \frac{F_{sheath+} - F_{sheath-}}{L_{\parallel}} \tag{2.18a}$$

$$\frac{1}{L_{\parallel}} \int_{sheath} V_{\parallel} \nabla_{\parallel} F = ? \tag{2.18b}$$

To address equation (2.18b) we need assume something about the parallel mode structure. The simplest and often physically justified assumption is that convected field quantities vary weakly along the field lines, $\nabla_{\parallel} F \approx 0$.

$$\frac{1}{L_{\parallel}} \int_{sheath} V_{\parallel} \nabla_{\parallel} F \approx 0 \tag{2.19}$$

2.2.7 $Log[n]$ or χ representation

A simple way to enforce positivity by considering a simple transformation

$$\chi = \log(n) \tag{2.20a}$$

$$n = e^{\chi} \tag{2.20b}$$

With this definition we can choose to evolve χ rather than n, it's straightforward to show the equations take a mildly different appearance, in particular the continuity equation takes the form:

$$\partial_t \chi + V_E \cdot \nabla \chi = \frac{2}{B} \hat{b} \times \hat{\kappa} \cdot (\nabla T_e - T_e \nabla \chi - \nabla \phi) - \nabla_{\parallel} \left(V_{e,\parallel} \right) + D_n \left(\nabla^2 \chi + (\nabla \chi)^2 \right) + \frac{S_n}{e^{\chi}}, \tag{2.21}$$

elsewhere n is replaced with e^{χ}.

$Log[n]$ representation was used extensively in this work, especially in examining steady state profiles where the flux-surface average density may vary by several orders of magnitude and turbulent coherent structures that can induce shocks that in traditional representations may generate unphysical negative densities.

2.3 Field line averaged equations

With discussion in section (2.2.6.1) in mind the field-line averaged version of equations (eqs. (2.2), (2.4) and (2.5)). These equations have been re-scaled by the Bohm gyro-radius $\rho_s = c_s/\Omega_i$, ion gyro-frequency Ω_i, and ion-acoustic speed $C_s = \sqrt{kT_{e,0}/m_i}$. We focus on sheath connected, far SOL blobs and thereby use the closure described in section 2.2.6, where elementary sheath theory gives the parallel current flow to the sheath but

parallel plasma resistivity is neglected.

$$\partial_t n + V_E \cdot \nabla n = \frac{g}{B}\left(\partial_y P_e - n\partial_y \phi\right) - \left(\frac{2}{L_\parallel}\right)\left(n T_e^{\frac{1}{2}}\right)\left(e^{\Lambda - \frac{\phi}{T_e}}\right) + D_n \nabla^2 n + S_n \tag{2.22a}$$

$$\partial_t(\nabla^2\phi) + V_E \cdot \nabla(\nabla^2\phi) = g\left(\frac{B}{n}\right)\partial_y P_e + \left(\frac{2}{L_\parallel}\right) B^2 T_e^{\frac{1}{2}}\left(1 - e^{\Lambda - \frac{\phi}{T_e}}\right) + D_\omega \nabla^4 \phi \tag{2.22b}$$

$$\partial_t T_e + V_E \cdot \nabla T_e = g\left(\frac{2}{3}\frac{T_e}{Bn}\right)\left(\partial_y P_e - n\partial_y\phi + \frac{5}{2}n\partial_y T_e\right) - \left(\frac{2}{L_\parallel}\right)\frac{2T_e^{\frac{3}{2}}}{3}\left((1+\beta)e^{\Lambda - \frac{\phi}{T_e}} - \beta\right) + S_{T_e} \tag{2.22c}$$

(2.22)

One shortcoming of a 2D reduced model is that it is unable to account for the variation of the curvature along the field lines and variations in the parallel mode structure. Resolving the parallel mode structure requires a full three dimensional simulation [64], however fixing $k_\parallel$ at the most unstable wavenumber as given by analytic theory is one alternative. When the sheath-decoupled structures with $k_\parallel \neq 0$ are considered both driftwaves and interchange turbulence enter the physical picture. Recent work [2] indicates substantial qualitative changes in the behavior of this system when this full three dimensional, drift-wave inclusive, picture is taken into account. The simplifying nature of the 2D model, by contrast, enables a greater focus on properties that are independent of the 3D geometry of the SOL. As pointed out by B.Li [47] for shorter connection lengths ($L_\parallel < 100m$) simple linear analysis show that interchange instabilities dominate - justifying the application of a dimenisionally reduced 2D model.

2.4 Linear analysis

We consider the linear mode structure and specifically the influence that consistent inclusion of curvature drive terms in all equations has on the growth of the dominant mode. Linearizing the 2D reduced model near some characteristic background profiles, with length scales L_n,L_T and so on, where $n_0(r) = n_0 e^{-\frac{r}{L_n}}$, $T_{e,0}(r) = T_{e,0} e^{-\frac{r}{L_T}}$, we can examine the growth rates and mode structure in the resulting dispersion relation. Particular attention is paid to the linear response in the large $k_\perp$ limit, where the nature of the linear response may demand special attention to numerics.

Linearizing the normalized equation 2.22, taking the local approximation, and some algebraic simplification yields a set of linear equations

$$\omega n + \underbrace{\frac{2}{R}}_{g_{eff}} k\left(-n + \phi - \mathcal{T}_e\right) + k\left(-\frac{\phi}{L_n} + \frac{n\Lambda}{L_\phi}\right) + i\alpha\left(n - \phi + \Lambda\mathcal{T}_e\right) + ik^2\mathcal{D}n = 0 \tag{2.23a}$$

$$\omega\phi + \frac{\Lambda\phi}{kL_\phi^3} + \frac{\left(-1 + k^2R^2\right)\Lambda\phi}{kR^2L_\phi} - \frac{2}{kR}\left(n - \frac{\Lambda\phi}{L_\phi^2} + \mathcal{T}_e\right) + i\frac{\alpha\left(\phi - \Lambda\mathcal{T}_e\right)}{k^2} + ik^2\mathcal{D}\phi = 0 \tag{2.23b}$$

$$\omega\mathcal{T}_e + \frac{2}{R}k\left(-\frac{2n}{3} + \frac{2\phi}{3} - \frac{7\mathcal{T}_e}{3}\right) + k\left(-\frac{\phi}{L_T} + \frac{\Lambda\mathcal{T}_e}{L_\phi}\right) + i\frac{2}{3}\alpha(1+\beta)\left(\phi - \Lambda\mathcal{T}_e\right) + ik^2\mathcal{D}\mathcal{T}_e = 0 \tag{2.23c}$$

(2.23)

These equations yield a cubic dispersion relation that can be solved analytically for the eigenfrequency ω. In the following subsections we will examine the solutions of this equation in simple limits.

2.4.1 Thermalized electron limit

If we consider thermalized electrons with electron temperature fluctuations, T_e, set to 0 and for the moment neglect both diffusion and curvature drive in the continuity equation we recover the linear growth rate for commonly given SOL 2-field interchange driven system. The relatively long expression should not obscure the basic physical fact that the instability is analogous to that observed in an inverted pendulum where $\gamma \propto \sqrt{\frac{g}{L}}$ with the effective gravity now set by the centrifugal force experienced by a fluid element $g_{eff} \approx \frac{v_i^2}{R}$, yielding a normalized growth rate $\tilde{\gamma} = \sqrt{\frac{1}{RL}}$, which is boxed here for emphasis.

$$\gamma = -\frac{1}{2}\left(1 + \frac{1}{k^2}\right)\alpha + \sqrt{\frac{\left(-1+k^2\right)^2\alpha^2}{4k^4} + \boxed{\frac{2}{RL_n}}} \qquad \text{if } \mathcal{T}_e = 0 \tag{2.24}$$

For convenience we associate $\sqrt{\frac{2}{RL_n}}$ with γ_0, the most simple and physically important expression of the linear growth rate associated with this system. Adding diffusion is necessary to control the amplitude of large-k (wavenumber) fluctuations, and saturate any present turbulence at some well resolved wavenumber. Consider the complex eigenvalue, ω, that satisfies equation (2.23), in the limit of negligible parallel dissipation. We can see that in this limit, for large wavenumber $k_\perp$, inclusion of curvature drifts in the continuity suppresses the linear growth rate, and perhaps less surprisingly shifts the real part of the dominant eigenfrequency by some characteristic curvature drift frequency, $\frac{2k}{R}$.

$$\lim_{\substack{\alpha\to 0\\ k\to\infty}} \omega = \frac{2k}{R} - i\alpha + \mathcal{O}[\alpha]^2 + \mathcal{O}[\frac{1}{k}]^1 \qquad \text{with} \propto g_{eff} \text{ term in the } n \text{ eqn.} \tag{2.25}$$

$$\lim_{\substack{\alpha\to 0\\ k\to\infty}} \omega = i\left(\gamma_0 - \frac{\alpha}{2}\right) + \mathcal{O}[\alpha]^2 + \mathcal{O}[\frac{1}{k}]^1 \qquad \text{without} \propto g_{eff} \text{ term in the } n \text{ eqn.} \tag{2.26}$$

$$\tag{2.27}$$

2.4.2 Non-thermalized blobs

To discuss energy transport in the SOL of a flux driven system our description must evolve a temperature field rather that ignore temperature fluctuations or fix a temperature profile[56]. Inclusion of temperature does change the linear response picture, and necessitate the inclusion of a diffusive term in the electron temperature equation.

$$\lim_{k>>1} \omega \approx i\alpha\left(\frac{2}{3}1.71\Lambda - 1\right) + \frac{14}{3}\frac{k}{R} - ik^2\mathcal{D}_{\mathcal{T}} + \mathcal{O}[\frac{1}{k}]^3 \qquad \text{with } \mathcal{T}_e \tag{2.28}$$

In figure (2.2) we observe that the exclusion of diamagnetic terms coupled with negligible diffusion (red dashed curve) results in a linear response without a well defined dominant mode. The importance of selecting a correct value of diffusion in modeling single blob dynamics has been shown by A. Aydemir [3], this simple linear analysis suggests that including diamagnetic terms in all equations seems to be similarly important.

2.5 Reference State and Numerical details

We are interested in examining the effect $\mathbf{E_0} \times \mathbf{B_0}$ velocity shear has on the observed turbulence in the Helimak. We performed series of simulations based on equations

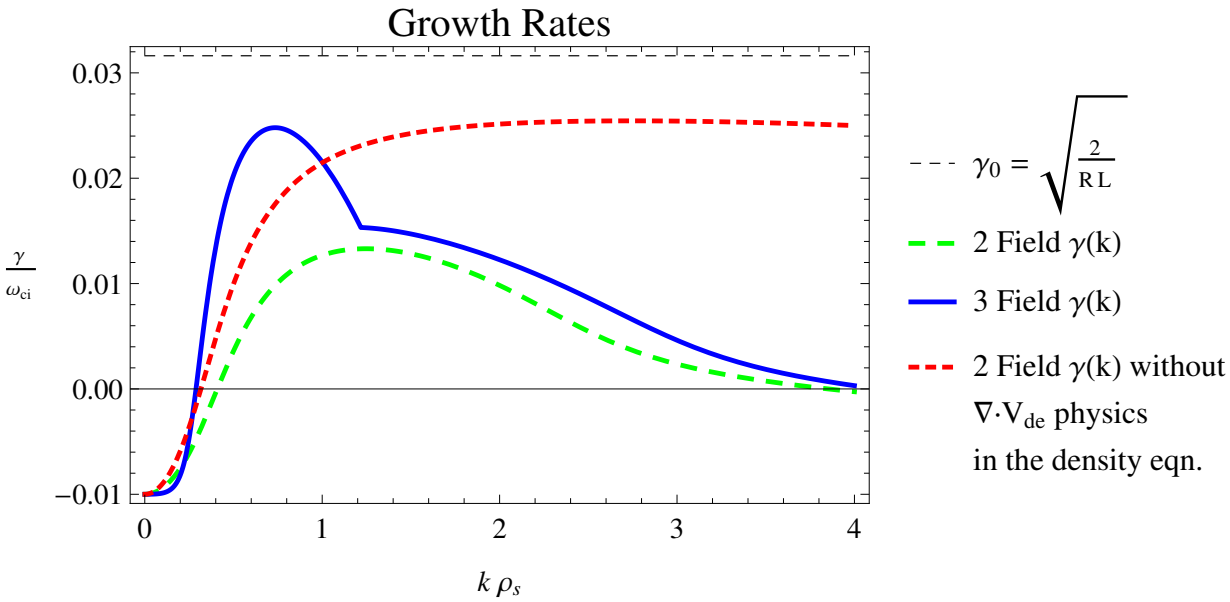

Figure 2.2: Dominant growth rate γ for a few variations of the linear dispersion relation equation 2.23. The normalized diffusion coefficients have been set to $D_n = D_\omega = 1 \times 10^{-4}$, the temperature diffusion coefficient has been set to $D_T = 1 \times 10^{-2}$. Other normalized parameters have been set to values characteristic of a typical SOL with: $\alpha = 1 \times 10^{-2}$, $g_{eff} = 5 \times 10^{-1}$, and with normalized gradient length scales $L_n = 20$ and $L_T = 20$.

2.22 using the BOUT++([23, 79, 22]) framework to discretize and evolve equation (3.2). The framework uses a local polynomial approximation to compute derivatives along the x coordinate, pseudo-spectral methods to compute derivatives along the y coordinate, and a CVODE([15]) solver to advance the fields in time. A set of Helimak-like parameters was selected as summarized in table 2.2. Note that we do not attempt to simulate the full device in the vertical dimension but consider a vertical segment corresponding to roughly $\frac{1}{3}$ of the device height. Neumann boundary conditions with zero gradient were selected for the radial ends of the simulation domain, allowing the mean profile value to move unconstrained except for the value of the slope. Enforcing Dirichlet boundary conditions that are sufficiently different from the field values directly to the interior may cause sharp, numerically troublesome gradients, benign but unrealistic regions of stabilizing curvature in the far SOL or equally nonphysical sinks that may drive cold coherent structures into radially inward.

Parameter	Value
mesh size:	$nx \times ny = 720 \times 512$
physical dimensions:	$L_x \times L_y = 70\rho_s \times 30\rho_s$
curvature drive:	$g_{eff} \approx 1 \times 10^{-2} - 3 \times 10^{-2}$
parallel dissipation:	$\alpha \approx 5 \times 10^{-4} - 1 \times 10^{-3}$
diffusion :	$D_n = D_\omega = D_{T_e} = 1 \times 10^{-2}$
magnetic field geometry:	$\frac{B_{0,T}}{B_p} = 10$
boundary conditions:	$\partial_x n = \partial_x T_e = 0$ on both ends in x

Table 2.2: Typical Helimak-like simulation parameters

In experimental realization the plasma is generated from a neutral gas via electron cyclotron resonance heating (ECRH) at a radius where the natural electron cyclotron frequency and the frequency of the external microwave source match (2.45 GHz). Due to

incomplete energy deposition at the cyclotron resonance layer the somewhat diminished microwave beam will continue on radially outward and impede on the upper hybrid resonance layer. Due to the turbulent nature of system and density dependence in the upper hybrid resonance condition there may be multiple positions where the resonance condition will be met and additional energy deposition and neutral ionization takes place. We opt to not address this potentially important source of error and model the source with a simple Gaussian with a well defined stationary maximum for both density and temperature.

Since the parallel losses are in fact the primary loss mechanism here we can easily show that the radial integral of externally applied sources must be of the order $\mathcal{O}[\alpha \times L_x]$ to balance the losses. One can solve a simplified version of equations 2.22 to verify this. Both density and temperature source terms, S_n and S_{T_e} respectively, were set to

$$S_n = S_{T_e} = \frac{\alpha L_x}{\sqrt{2\pi\sigma^2}} e^{-\left(\frac{x-x_0}{2\sigma}\right)^2}, \tag{2.29}$$

with $x_0 = 56\rho_s$ and $\sigma \approx 6\rho_s$. As pictured in figures 2.3 the mean values of normalized T_e and n equilibrium settle on values of order unity, implying that sources and sinks are well balanced in this system.

The cited range of values for curvature driven effective gravity and parallel dissipation in table 2.2, g_{eff} and α respectively, reflect our choice to vary these parameters in accord with the magnetic geometry. Specifically

$$\alpha = \frac{2\rho_s}{L_\parallel}, \text{ where } L_\parallel = \frac{H}{\rho_s}\sqrt{1 + \left(\frac{B_{T0}R_{R,0}}{B_P R}\right)^2}. \tag{2.30}$$

As mentioned in section 2.3 we are working in the sheath connected limit and therefore consider a relatively short connections length of about 50 meters. Much longer connections lengths from the experimentally accessible range of length values available to the Helimak would generally require resolving the parallel mode structure and are better treated with a full 3D geometry.

Figure 2.3 displays the mean normalized (averaged in both time and vertical directions) density and temperature profiles.

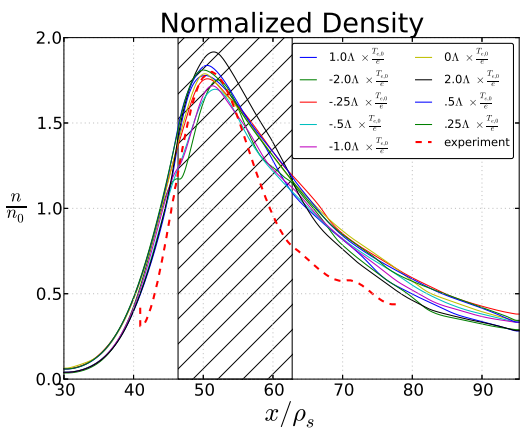

(a) As we consider several bias voltages on the second endplate the equilibrium density relaxes to the profiles pictured.

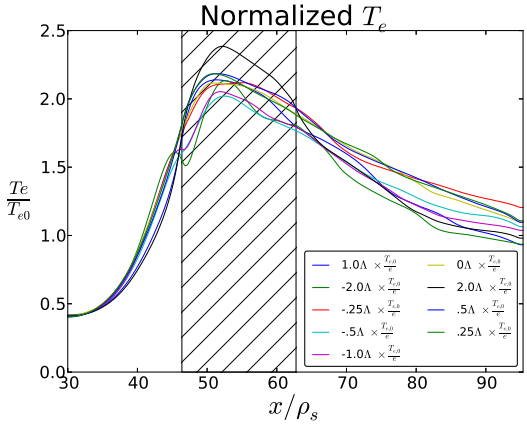

(b) Similarly to the density profiles the external biasing only weakly affects the temperature profile.

Figure 2.3: Both density and temperature profiles equilibrate on mean values on the order unity, and are only weakly affected by external biasing. The region where a potential bias was applied is dashed. The mean density and temperature peaks are shifted inward rather than being aligned with the source peak, with blob facilitated transport on the bad curvature side chiefly responsible for this feature. We see that the experimental density profile is qualitatively similar to the simulation results, the apparent discrepancy can possibly be attributed to source terms in eqs. (2.2) and (2.5) that may overestimate turbulent broadening. The experimental and computational profiles can also be brought into very close agreement by reducing the spatial normalization ρ_s by about 20% from the experimentally reported value of 2cm, under this interpretation simulations appear to correspond to a somewhat warmer plasma than the experiment.

2.6 Numerical Studies of E $\times$ B shear and density fluctuations

As pointed out in section 2.2 we opt to evolve the entire bulk of the fields considered rather than simply evolve perturbation around some fixed equilibrium profile. A typical simulation initialized the fields n, ϖ, T_e with sum of a flat profiles and a very large σ Gaussian perturbation. An initial condition with a large spatial footprint but one that

still has a multi-component Fourier decomposition ensures that a number of modes represented is reasonably large, the initial gradients are gentle and avoid numerical issues, and that the interchange instability has a maximum growth at a wavelength smaller than the initial blob size. The net effect is that the initial condition destabilizes quickly and breaks up into smaller structures that are representative of the physics modeled - not the choice of initial conditions. Both the initial flat background and the Gaussian perturbation typically had a normalized amplitude of $\frac{1}{10}$.

As we probe the relationship between velocity shear and turbulence we systematically vary the bias potential in increments of $\frac{\Lambda}{2}$ of normalized potential, corresponding to unnormalized increments of $\frac{\Lambda\langle T_{e,0}\rangle}{2e} \approx 10\ eV$ for typical T_e profile values. As the poloidially averaged shear rate , $\partial_x V_x$, approximately exceeds the interchange rate we expect an inverse cascade process to stabilize interchange modes, shorten radial correlation lengths, and decrease fluctuation levels [71]. This theoretical prediction of shear facilitated stabilization has not been conclusively observed at the Texas Helimak.

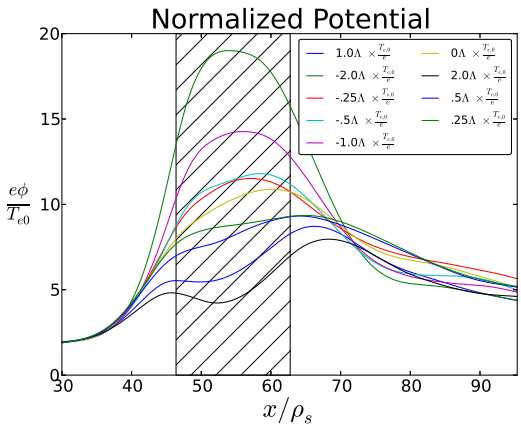

(a) The normalized potential profiles as we consider a a number of bias offsets.

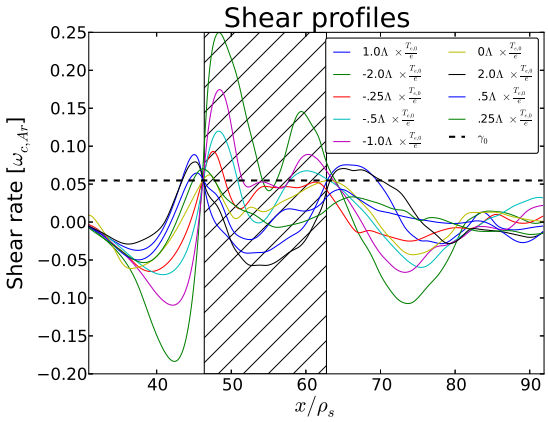

(b) The corresponding shear, the maximum value of the interchange growth rate (dashed) is shown for scale.

Figure 2.4: Examining the mean potential for saturated turbulent states we see that equation (2.15), provides a useful rule of thumb in estimating the mean potential. The shear rates pictured in figure (b) seem to pivot around the estimated maximum value of the interchange rate on both interchange stable and unstable sides of the density maximum. This observation suggests a strong interaction between Kelvin-Helmholtz and interchange dynamics in this system.

We see in figure 2.4 as we increase a negative bias on the second plate the resulting plasma potential trends up, generally increasing $\mathbf{E_0} \times \mathbf{B_0}$ flow shear immediately outside the biased region, in agreement with equation (2.15). To review, in section 2.2.6, we discuss how external biasing will be reflected in the final plasma potential profile, and here we see that the approximate expression

$$\phi_s(x) \approx \frac{\Lambda T_e(x)}{e} - \phi_w(x), \tag{2.31}$$

is in fact satisfied in the simulation.

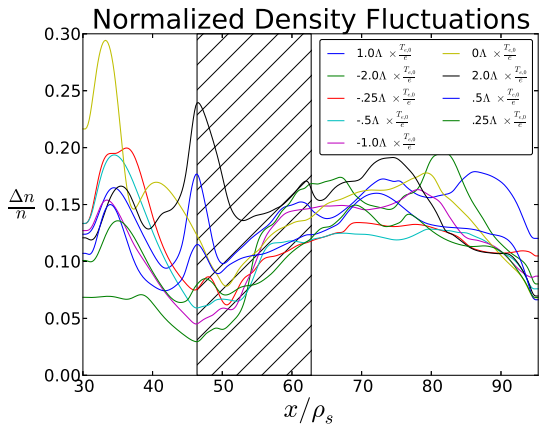

(a) Normalized density fluctuations for several bias voltage values.

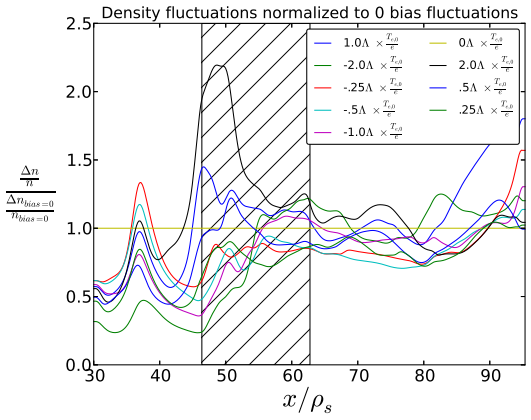

(b) Density fluctuations show overall suppression for mostly negative bias voltages, however radially extended regions where suppression is observed for all but the largest positive bias voltages are observed.

Figure 2.5

2.7 Summary of current findings

We considered a 2D model applicable to sheath connected interchange turbulence in the Texas Helimak. Our chosen model is expected to yield best agreement for relatively short connection length regimes where $L_{\|} < 100$ meters. Simple analysis of fluctuation levels as quantified by rms values of density fluctuations shows that profiles that maximize $\mathbf{E_0} \times \mathbf{B_0}$ flow shear can significantly reduce the mean amplitude of the density fluctuations as pictured in figure 2.6. The simulated temperature profile is more peaked than the experimentally observed profile raising the possibility that some cross-field transport channel is neglected in our temperature equation or that the complex nature of turbu-

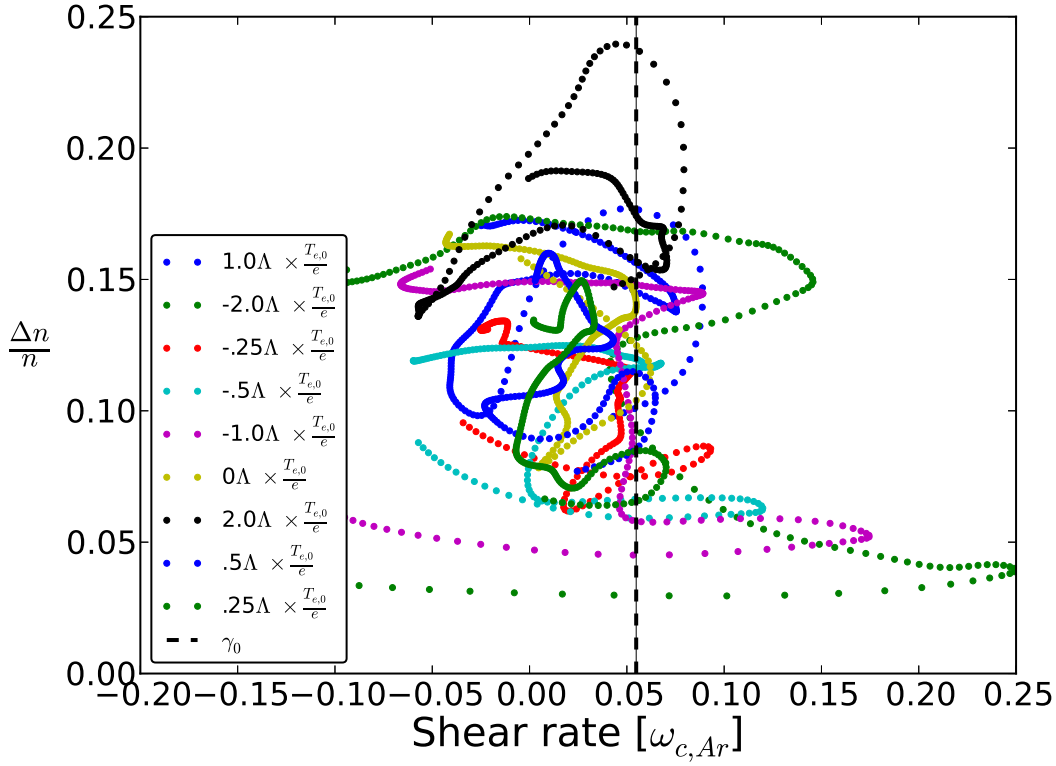

Figure 2.6: While there is an overall trend of turbulence suppression associated with increased flow shear the observed variance is very large.

lently broadened power deposition is not correctly represented. In contrast, the density profiles appear somewhat more broad than the corresponding experimental profile, again suggesting an incorrect account of the cross-field transport, source width, or a spatial displacement rescaling that is more appropriate for a warmer, larger ρ_s, plasma. Interaction between flow shear and interchange instability appears to be important, with the interchange rate coinciding with a pivot point for shear rates in figure 2.4 and shear rates in excess of of the interchange rate appearing to limit normalized density fluctuations in figure 2.6. Additional work is required to positively identify Kelvin-Helmholtz instabilities, interchange driven blobs, and examine the interaction between the two phenomena.

Chapter 3

SOL system with field-line chaos and thermalized electrons[1]

Naturally occurring error fields as well as resonant magnetic perturbations applied for stability control are known to cause magnetic field-line chaos in the scrape-off layer (SOL) region of tokamaks. Here, 2D simulations are used to investigate the effect of the field-line chaos on the SOL and in particular on its width and peak particle flux. The chaos enters the SOL dynamics through the connection length, which is evaluated using a Poincaré map. The variation of experimentally relevant quantities, such as the SOL gradient length scale and the intermittency of the particle flux in the SOL, is described as a function of the strength of the magnetic perturbation. It is found that the effect of the chaos is to broaden the profile of the sheath-loss coefficient, which is proportional to the inverse connection length. That is, the SOL transport in a chaotic field is equivalent to that in a model where the sheath-loss coefficient is replaced by its average over the unperturbed flux surfaces. A 2D model with uniform electron temperature does not include the effects of magnetic shear, enhanced cross-field transport or chaotic features other than the parallel connection length.

[1]This chapter is based on previously published work [52]. The author acknowledges multiple revisions and discussions with Dr. Francois Waelbroeck and Dr. Craig Michoski. The author is grateful to Dr. Wendell Horton's insightful feedback.

In diverted tokamaks, the separatrix defines the boundary between open and closed flux surfaces and acts as a riverbed for the scrape-off layer (SOL). In the SOL, the flow across the magnetic field balances the parallel streaming along the field towards the plasma-facing components (PFC). A picture of how tokamak turbulence and transport in the SOL scale with experimentally controllable parameters is necessary to minimize peak heat and particle flux loads on the PFC,[42] to minimize introduction of impurities, and to simultaneously maintain conditions that are consistent with global plasma confinement.[28, 46, 43, 18] In the presence of edge-resonant non-axisymmetric perturbations, however, the separatrix is readily shattered and replaced by a region exhibiting field-line chaos, or magnetic stochasticity, which manifests its presence by the splitting of the separatrix footprints.[80] Field-line chaos can be introduced by deliberately applied resonant Magnetic Perturbations (RMPs) [39], ergodic magnetic limiters [49, 33] and naturally-occurring instabilities. RMPs have been the subject of intense recent interest for their use in controlling edge localized modes by keeping the edge pedestal conditions below some critical threshold and by effectively replacing impulsive intermittent ELM transport with a series of smaller less disruptive transport events, or even by achieving full suppression.[25]

While the turbulent SOL has a complex three dimensional geometry, its physics is dominated by curvature-driven interchange instabilities characterized by a short extension across but a long extension along the field lines.[18] Following standard practice, we average vorticity and density equations along the field-aligned dimension and work in the resulting 2D plane normal to the field-lines. Excluding regimes where full drift-wave physics has a strong influence on the dynamics [64, 2, 1], this dimensionally-reduced ap-

proach has provided experimentally validated descriptions of turbulent transport, interplay between zonal flows and turbulence,[57, 67, 83] creation of coherent structures, and SOL density length scales, among other results.[69, 44, 88, 17, 30, 57] End-losses along the field appear as a damping term in the density equation characterized by a coefficient α that is inversely proportional to the connection length $L_{\parallel}$:

$$\alpha = 2\rho_s / L_{\parallel} \tag{3.1}$$

In this chapter we specify $L_{\parallel}$ by a map that describes chaotic connection lengths in the region spanning the outer portions of the core and the SOL. To maintain the density in the presence of the end-losses, we include a particle source at the core-facing edge of the simulation domain. The resulting turbulence is thus flux-driven. The particle source can be thought of as modeling the injection of particles by gas feed, neutral beams, pellets and recycling.

It is generally accepted that cross field transport in the region between the plasma edge and the vessel wall is dominated by intermittent transport [7, 69, 31] mediated by coherent, radially propagating plasma filaments called blobs.[44, 10, 48, 29, 87] Typically the magnetic-curvature drift combined with the usual $\mathbf{E} \times \mathbf{B}$ convection will drive a blob radially outward (Fig. 3.1). Continuity and charge conservation equations govern their dynamics. Blobs provide a mechanism for radial transport of heat and momentum that greatly exceeds neoclassical predictions. The usefulness of blobs, as a concept, depends on their ability to survive long enough to affect transport and demonstrate a clear dependence of their properties on model plasma parameters. Blob lifetimes have been examined theoretically by Krasheninnikov [44] and other authors [56, 31] and experimentally

in tokamaks[10, 48] and other devices.[5, 76, 75] These studies have shown the existence of a most-stable blob size. The mechanisms underlying the interplay between parallel transport, diffusion, convective processes, and spontaneous formation of blobs affects the width of the SOL layer and the intermittency of transport. These mechanisms have been studied in some detail.[18, 30, 3, 2, 67]

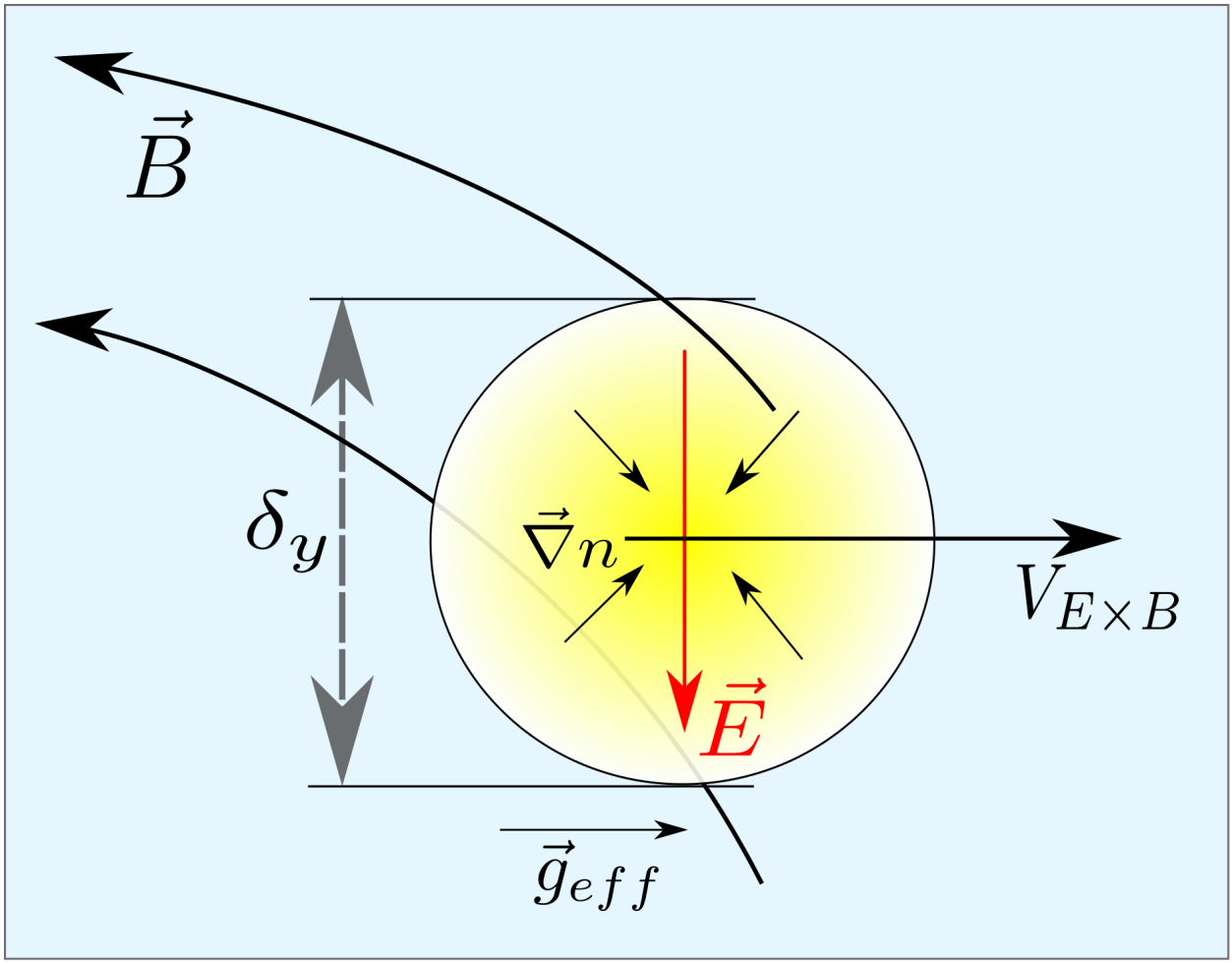

Figure 3.1: A simple blob with key forces, length scales and directions

In this paper we examine how magnetic chaos, modeled with a chaotic map that mimics the application of static RMPs, changes statistical characterization of blobs and the scaling of their properties with plasma parameters. As an example of how our current understanding of blob behavior may be challenged by the presence of chaos, consider the simplest analytic prediction of radial blob velocity:$V_x \propto L_\parallel/(R\delta_y^2)$, where δ_y is the blob size (Fig. 3.1). With the addition of a chaotic field, there will be large variations in the $L_\parallel$ value over the spatial footprint of the blob - possibly affecting its coherence and thus the mean particle transport and intermittency of density fluctuations. From previous work we also know that for a constant sheath-loss coefficient α there is a strong selection for a specific blob size.[3, 44] It is natural to ask whether magnetic chaos might seed blobs of different sizes, or favor hole creation over blob creation. Such effects on blob dynamics would clearly affect the observed density scaling distance in the SOL density profile. The aim of the present paper is to answer these questions within the framework of the 2D model of SOL transport.

The remainder of this chapter is organized as follows. In Sec. 3.1, we describe the formulation of the problem and some simple analytic considerations. In Sec. 3.2, we review the results for unperturbed SOL dynamics and use this review to verify our code. We then examine the effect of the field-line chaos in Sec. 3.3, with particular attention to the scaling of the density length-scale and the selection of the dominant blob size. We conclude by summarizing and discussing our results in Sec. 3.4 .

3.1 Formulation and Analytic considerations

We use a simple two fluid interchange model that nonetheless contains many of the most important features: curvature and density gradient drifts, convective nonlinearities, blob formation, and a parallel closure scheme that is able to model both closed and open field lines. Similar models have a been used by many authors to study SOL turbulence, zonal flows and transport in both mirror machines and tokamaks edge plasmas.[2, 89, 18, 3]

The equations used here have been normalized by the gyro-radius $\rho_s = c_s/\Omega_i$, ion gyro-frequency Ω_i, and ion-acoustic speed $c_s = \sqrt{kT_e/m_i}$. They are

$$\partial_t n + V_E \cdot \nabla n - D_n \nabla^2 n \ + \alpha n = S_n, \tag{3.2a}$$

$$\partial_t \varpi + V_E \cdot \nabla \varpi - D_\varpi \nabla^2 \varpi - \alpha \phi - \beta \frac{(b \cdot \nabla x \times \nabla n)}{n} = S_\varpi, \tag{3.2b}$$

$$\varpi = \nabla^2 \phi, \tag{3.2c}$$

$$V_E = b \times \nabla \phi, \tag{3.2d}$$

$$\beta = \frac{2\rho_s}{R_0} \text{ and } \alpha = \frac{2\rho_s}{L_\parallel} \tag{3.2e}$$

. The loss terms containing the coefficient α come from averaging the parallel current and velocities given by elementary sheath theory. Notice that we assume no scale-separation between some background and a perturbed portion. This is consistent with the observed character of the SOL layer. External density and momentum sources can be specified with S_n and S_ϖ respectively. In this work we set $S_\varpi = 0$. We will discuss the choice of S_n in section 3.1.3.

In arriving at equation (3.2), the full three dimensional geometry is reduced to two dimensions by averaging along the field lines, where we take the flute approximation [65]

and assume that all introduced quantities vary weakly along uniform magnetic field lines (*i.e.* the blobs are interchange-like). The influence of RMPs is then reflected in the parallel connection length to the divertor that enters into the α parameter of equation (3.2).

Note that α, the inverse of the total escape path, is in fact the only place magnetic geometry enters our system of equations. Local changes in magnetic shear and enhanced cross-field transport due to magnetic chaos are neglected in this work. Enhanced cross-field diffusion could be represented empirically with an additional diffusive transport channel, $D_{chaos}(x, y)\nabla^2 n$, in the density equation. A more detailed analysis of how varying the overall diffusion coefficient changes blob coherence and overall transport has been presented by A.Aydemir [3] and others [18, 88]. Additionally note that by fixing the electron temperature at a constant reference value our equilibrium sheath potential is fixed as well, in a more realistic realization we expect an equilibrium with a radially varying equilibrium sheath potential, $\phi_0(x) = e\Lambda T_e(x)$, and a subsequent equilibrium $\mathbf{E_0} \times \mathbf{B_0}$ convection to be present.

We benchmark our numerical calculations with single blob dynamics and many-blob turbulence results from E. Garcia's, [30], and A.Y. Aydemir's work [3]. Some pre-existing published result can be reexamined with the presence of chaos in mind. We can For example, how does the previously posited and observed strong selection for a specific blob size, [3, 44] , change in the presence of magnetic chaos? Does chaos seed blobs or holes? Does it break up blobs or otherwise change the average blob size as compared to the laminar, flux-surface averaged, case? How does the observed e-folding distance in SOL density profile differ between cases with and without magnetic chaos? What effect, if any, does magnetic chaos have on the intermittency of density fluctuations? The purpose

of this work is to address these questions.

We observe that radial transport in this simpler edge region model, with constant coefficients, is dominated by blobs of specific size. The observed e-folding length is only weakly affected by the state of the plasma at the interface where blob birth takes place, once a sheath-connected blob is established. However an introduction of a chaotic interface where externally introduced magnetic fields deform, or even break up, what was the last closed flux surface can effectively encourage blob formation over a wider radial region and consequently change the observed mean density profile. Similarly we observe that the introduction of chaotic field lines and generation of a magnetic mixing layer can increase the width of the transition region that connects the internal region with weak parallel dissipation (often with strong zonal flow) and the far SOL layer where a well defined e-folding length and a clear dominant blob size is evident. We compute probability density functions (PDFs) for the observed density fluctuations to see that a chaotic connection length will generally encourage less intermittency in the density fluctuation, as compared to an abrupt transition from closed to open field lines.

Given that experimentally observed coherent structures have amplitudes that are of order unity compared to background, there is no way to justify differentiating between an equilibrium background and fluctuations, other than perhaps in the context of linear analysis and linear numerical verification of growth rates. Rather than consider some background density profile that drives fluctuations we consider a particle source on the core edge of the domain that has been selected to be of size that is compatible the physics of our system.

3.1.1 Geometry

While BOUT++ is designed primarily for field-aligned, non-orthogonal coordinates, it also allows for simulations in slab geometry. A shortcoming of the 2D slab model is that it is unable to account for the variation of the curvature along the field lines or for the resulting variation in the mode structure. Various estimates of the parallel wavenumber can be made.[89] Resolving the parallel mode structure requires a full three dimensional simulation.[64] Recent work [2] indicates substantial qualitative changes in the behavior of this system when the full three dimensional picture is taken into account. The simplifying nature of the 2D model, by contrast, enables a greater focus on properties that are independent of the 3D geometry of the SOL. Some consquences of this reduction are discussed in section 3.4.

3.1.2 RMPs and the Ullmann Map

Magnetic fields have a field-line structure governed by Hamilton's equations, with the toroidal angle playing the role of time. The field lines of axisymmetric equilibria lie on nested toroidal surfaces, constituting integrable Hamiltonian systems, and perturbations of such axisymmetric equilibria are naturally described by Poincaré sections, the intersection of field lines with a poloidal section. The Ullmann map [77, 63] is a Poincaré magnetic field line map that was created to study the effects of an ergodic divertor on toroidal plasmas. Repeated application allows us to assign a parallel connection length value based on the number of applications necessary for a given field line to hit the divertor. One advantage of this map over some others is that it is characterized in terms of experimental quantities such as major and minor radius, I_{ext}/I_p and some safety factor,

$q(r)$.

The connection lengths are said to exhibit chaos when two neighboring points are traversed by field lines that follow very different trajectories. For example, one field line may quickly terminate on the divertor or the wall while another may stay trapped. A sheath-loss coefficient α may be assigned based on Eq. (3.1) and this computed chaotic parallel connection length.

The Ullmann map [77] is a composition of a map with good flux surfaces, where

$$r_{n+1} = \frac{r_n}{1 - a_1 sin\theta_n}, \tag{3.3a}$$

$$\theta_{n+1} = \theta_n + \frac{2\pi}{q_{eq}(r_{n+1})} + a_1 cos\theta_n, \tag{3.3b}$$

and a perturbation map, given by

$$r_n = r_{n+1} + \frac{mC\epsilon b}{m-1}\left(\frac{r_{n+1}}{b}\right)^{m-1} sin\left(m\theta_n\right), \tag{3.4a}$$

$$\theta_{n+1} = \theta_n - C\epsilon\left(\frac{r_{n+1}}{b}\right)^{m-2} cos\left(m\theta_n\right). \tag{3.4b}$$

where q is the safety factor, C is a geometric factor, and ϵ is current in the external coil normalized by the plasma current

$$C = \frac{2mla^2}{R_0 b^2 q_a}, \tag{3.5a}$$

$$\epsilon = \frac{I_l}{I_p}, \tag{3.5b}$$

with $m = 2, 3, ...$ Given some effective minor radius a we can approximate the field-line length once we know how many applications of the map connect a given point to the divertor:

$$L_{\|} \approx q(a) 2\pi a N_{turns} \tag{3.6}$$

Ultimately what enters equation (3.2) is the inverse of this parallel connection length, $\alpha = 2\rho_s/L_\parallel$.

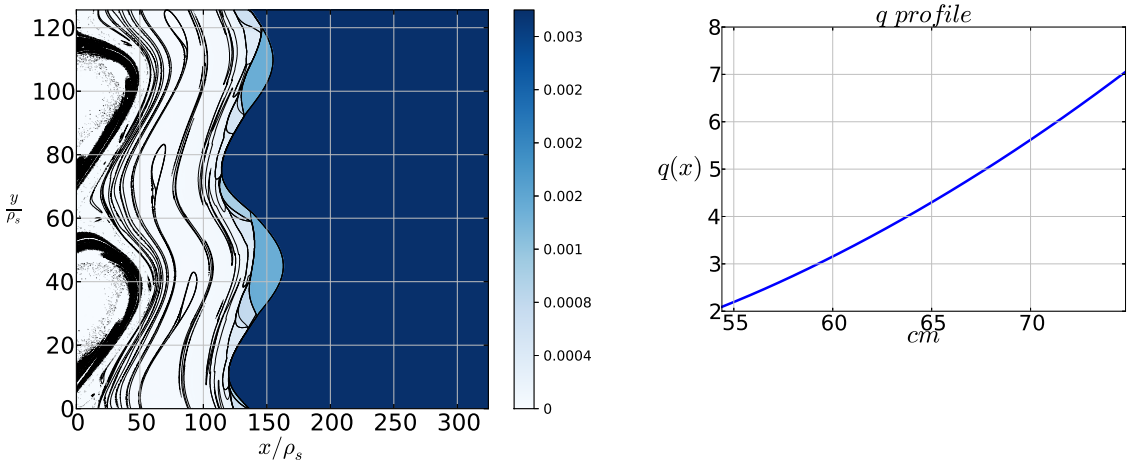

Figure 3.2: Contour plot of the inverse connection length, α, associated with magnetic chaos generated by the Ullmann map and the corresponding q profile of the left. Escape basins appear as darker regions, whereas trapped regions appear white and have $\alpha = 0$. Note that the contour values change discretely. A few hundred applications of the map are typically sufficient to map out escape basins and trapped field-lines for the resolutions considered.

To fix the parameters used in this study we adopt an NSTX-like geometry, with minor radius = 68 cm, plasma radius = 60 cm, external coil size =10 cm, R_0 = 85 cm, a_1 =-.01, and consider $I_{ext}/I_p = \epsilon = 0, .1, .2, .3$. We use the map to fix $\alpha(x, y)$ for the duration of the run. The resulting distribution of α values is shown in Fig. 3.2.

For the parameters selected the typical radial excursion of a chaotic field line is on the order of $\mathcal{O}[1cm]$, which for typical values of ρ_s translates into radial values of $\mathcal{O}[3\rho_s - 10\rho_s]$. Note that given a typical blob size, a^*, as discussed in section (3.3.2), the regimes we consider are one where the typical radial excursion, $\delta r \gtrsim a^*$, as well as a reference

case where $\delta r = 0$. In regimes where delta $\delta r < a^*$ calculating localized enhancements to cross-field transport may be a more appropriate strategy. The size of the typical radial excursion does not appear explicitly in the current model, only the total connection length does. As discussed in section 3.1.2.1 chaotic features beyond the net connection length can be included in the overall discription, but for the parameters considered here it may be be necessary.

From a macroscopic point of view, one of the effects of the magnetic field chaos is to broaden the transition between closed field lines and open field lines, which appears in an axisymmetric system as a jump in the connection length $L_{\|}$. In order to distinguish the effect of the spatial fluctuations of $L_{\|}$ in a chaotic SOL field from the effect of the broadening of the transition, it is interesting to consider a model in which the chaotic inverse connection length is averaged over an unperturbed flux-surface. We will refer to this case, illustrated in Fig. 3.3, as the "smooth alpha" case.

3.1.2.1 Cross-Field Diffusion

While the diffusion coefficient does not come from Braginskii equation directly, it can estimated in number of ways. The simplest and perhaps the least realistic approach is assume a random walk in the magnetized limit.

$$D_{collision} \approx \frac{\nu_{ei}\rho_e}{2} \approx \times 10^{-(6-8)} \left(\rho_s^2 \omega_{ci}\right) \tag{3.7}$$

While we expect to resolve collective transport phenomena on scales larger that our chosen grid size, we cannot expect to resolve subscale turbulence. Turbulent Bohm

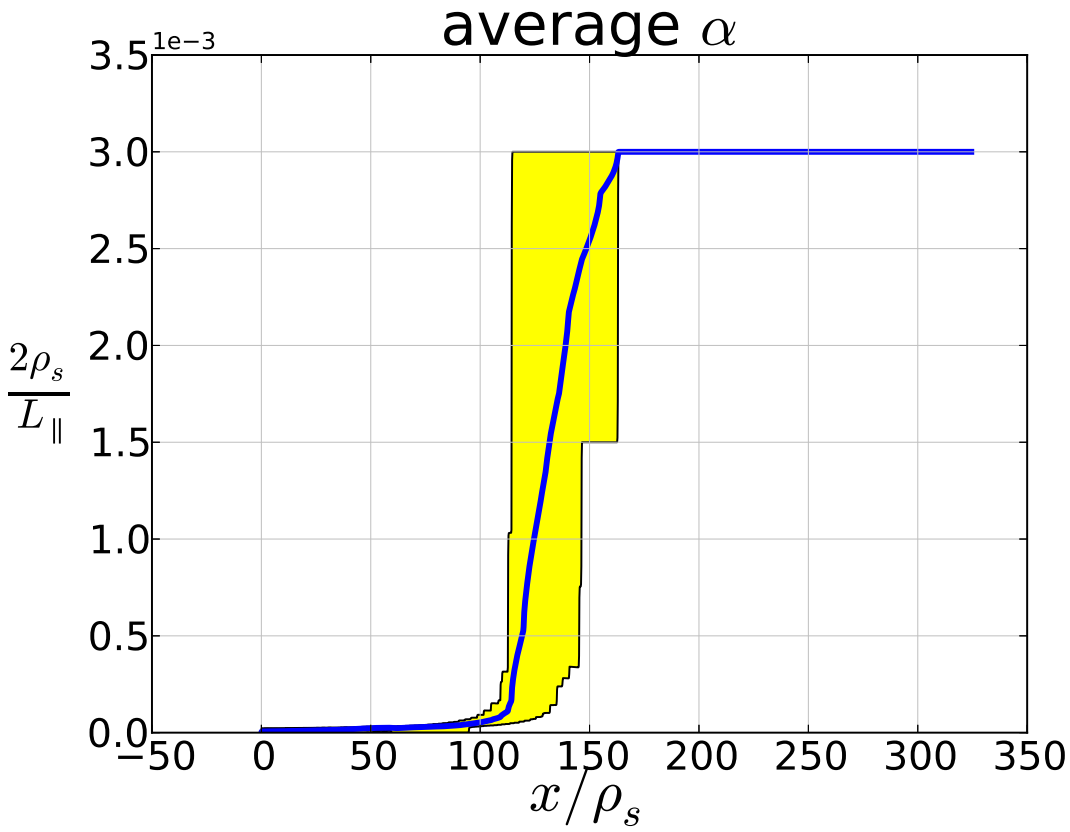

Figure 3.3: The flux-surface averaged α as a function of the radial position with the full range of α superimposed.

diffusion is the next best estimate after simple collisional diffusion [37, 6].

$$D^{Bohm} = \frac{\Delta x^2}{\tau}$$

Associating $\frac{\Delta x}{\tau}$ with the turbulent fluctuations in $\mathbf{E} \times \mathbf{B}$ velocity

$$\frac{\Delta x}{\tau} \approx \frac{\delta\Phi}{\Delta x B} \rightarrow D^{Bohm} \approx \frac{\delta\Phi}{B} \tag{3.8}$$

Turbulent fluctuations in the electric potential, $\delta\Phi$, can be related to the mean electron temperature with an approximate factor of $\frac{1}{16}$, $\delta\Phi \approx \frac{1}{16}\frac{T}{e}$. With respect to characteristic parameters of our plasma Bohm diffusion becomes

$$D^{Bohm} = \frac{1}{16}\left(\rho_s^2\omega_{ci}\right) \approx 5 \times 10^{-2}\left(\rho_s^2\omega_{ci}\right).$$

This estimate is comparable to that used in many 2D SOL simulations.

A natural question to ask is how much does parallel transport contribute to the cross-field transport in the 2D plane of interest by connecting a set of points with fast parallel transport. Specifically consider simple parallel diffusion, where thermal electrons move along some mean-free-path before colliding, where electron-ion collisions are the fastest relevant collision process. For typical SOL parameters this diffusivity exceeds any perpendicular transport processes by orders of magnitude, as shown in equation 3.9,

For a quasineutral plasma we can compute the composite parallel plasma diffusion from standard collisional diffusion and the resulting ambipolar electric field [6],

$$D_{\parallel} \approx \left(1 + \frac{T_e}{T_i}\right) V_{th,i}^2 \tau_i = \left(1 + \frac{T_i}{T_e}\right) C_s^2 \tau_i \approx C_s^2 \tau_i \gg C_s^2 \omega_{ci}^{-1}, \tag{3.9}$$

where for a magnetized plasma the ion collision frequencies are slow compared to the ion gyro-frequency, $\tau_i^{-1} = \nu_i \ll \omega_{ci}$. A similarly fast parallel vorticity diffusivity can be found. Given some typical magnetic field fluctuation, δB, an enhanced Rechester-Rosenbluth diffusivity in the plane normal to the field-lines can be estimated [27],

$$D_{R,R} \approx D_{\parallel} \left(\frac{\delta B}{B} \right)^2 . \tag{3.9}$$

Substituting ambipolar parallel diffusion from equation 3.9 and normalizing to time and displacement scales of ω_{ci}^{-1} and ρ_s respectively, yields a diffusion rate somewhat smaller than the diffusivity used in our simulations,

$$\widetilde{D_{R,R}} = \frac{\omega_{ci}}{\nu_i} \left(\frac{\delta B}{B} \right)^2 \approx (1 \times 10^{-4} - 1 \times 10^{-2}), \tag{3.9}$$

where $\frac{\omega_{ci}}{\nu_i} \approx 1 \times 10^3$ and $\frac{\delta B}{B} \approx 1 \times 10^{-3}$ have been estimated based on typical SOL and RMP parameters. The range of normalized Rechester-Rosenbluth diffusion values falls below the typical diffusion values used in the simulations performed here, suggesting that magnetic chaos facilitated cross-field diffusion can generally be neglected in this particular study. However, depending on the degree of magnetic chaos and collisionality of the plasma Rechester-Rosenbluth diffusion has the potential to greatly enhance cross-field transport.

3.1.3 Reference state

We are interested in characterizing intermittency and the SOL profile as a function of the RMP amplitude. Since we will be driving turbulence by introducing a particle source S_n on the core-side edge of the simulation, it is useful to consider how to select S_n in our model.

The primary density sink in our system is loss through the divertor sheaths (the αn term). If we account for the nonlinear terms through an anomalous diffusivity D_a and assume a source localized at the boundary of the simulation and of the form $S_n = S_0\,\Theta(x_\star - x)$, the profile of the average density will take the form

$$n(x) = n_0 e^{-x\sqrt{\frac{\alpha}{D_a}}} \text{ for } x > x_\star, \tag{3.9}$$

where $S_0 = 2n_0$. This simple result reflects the fact that the source must roughly balance the dominant sink, represented by the αn term in the density equation.

Note that without a particle source the equations are invariant under a change in the global background density, $n \to n + n_0$. The source strength thus has the effect of setting the background density for given D_a.

3.2 Unperturbed SOL Dynamics

Just as in a later Helimak study 2 we use the BOUT++ framework to evolve equation (3.2). To assess the reliability of our numerical tools we verify the linear dispersion relation in section(3.2.1) as well as verify that nonlinear analytic predictions favorably compare to the single blob dynamics of two other codes ([54], [30]) in section (3.2.2), and finally match published SOL width values [3] in section (3.2.3).

3.2.1 Linear Verification

We compare the growth rate of the SOL interchange mode as deduced from a simulation of a linearized version of equation (3.2) with the analytically derived growth rate γ. Expanding equation (3.2) to the lowest order in ϕ, u, n, setting $D_\omega = D_n$, and dropping

parallel dissipation in the density equation yields the analytic result

$$\gamma = -\frac{\left(\alpha + 2Dk_\perp^4\right)}{2k_\perp^2} + \sqrt{\left(\frac{\alpha}{2k_\perp^2}\right)^2 + \frac{\beta}{\ell_n}}. \tag{3.10}$$

The above expression for the growth rate shows that the mode is driven by the interchange term β/ℓ_n and is stabilized by dissipation for short wavelengths. The growth rate peaks for wavelengths of a few times the Larmor radius ρ_s.

For the numerical calculation, several γ^{-1} time increments may be required to converge on the solution, unless one sets the initial condition such that u, ϕ correspond to an eigenvector of the linearized version of equation (3.2). Fig. 3.4 shows that the simulations are in satisfactory agreement with the analytic dispersion relation.

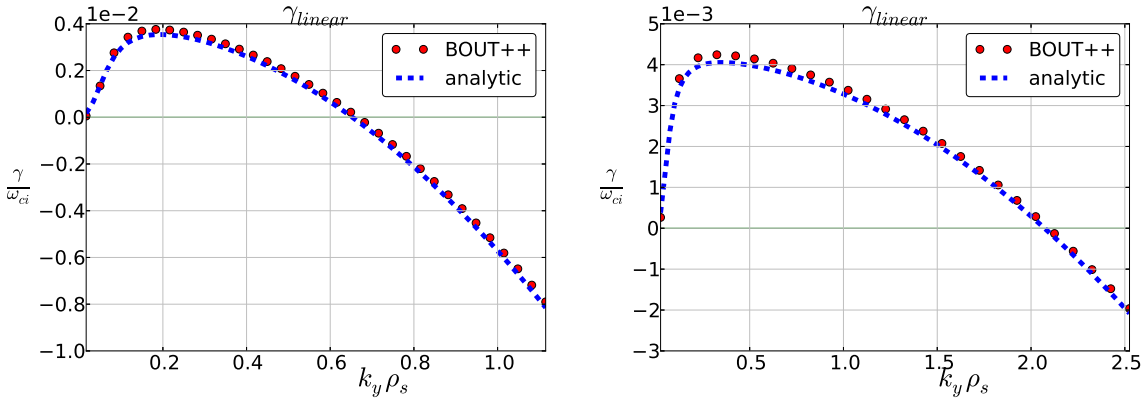

Figure 3.4: Growth rate γ as a function of the poloidal wavenumber k_y, where $D = \mu = 1 \times 10^{-2}$ and 1×10^{-3} on left and right charts respectively, $\beta = 6 \times 10^{-4}$, $\alpha = 3 \times 10^{-5}$. Good agreement between analytic theory and BOUT++ results is observed.

3.2.2 Single-blob dynamics

In their insightful paper, Garcia *et al.* (2006) ([30]) have shown how to characterize the motion of individual blobs by their center of mass. We have repeated some of their simulations using the initial and boundary conditions shown in Table (3.1). We chose a simulation domain large enough to keep the blob far away from the boundaries for the duration of the run. In particular, the size of the domain is such that changing boundary conditions between Dirichlet ($n_{x\ boundary} = 0$), and Neumann ($\partial_x n_{x\ boundary} = 0$), only weakly affects the history of the leading moments describing the blob.

Parameter	Value
N_x	1056
N_y	1024
L_x	60
L_y	40
$n(t=0)$	$e^{\frac{(x^2+y^2)}{2}}$
$u(t=0)$	0
BC_x	$\partial_x u = \partial_x n = 0$
BC_y	*periodic*
Ra	$10^{2,4,6}$

Table 3.1: Numerical Blob Parameters

Fig. 3.5 compares the evolution of the velocity of the center of mass as well as the maximum amplitude of the density in the blob. We find consistent agreement between the results of BOUT++ and those presented by Garcia *et al.* (2006) as well as with recent work by Michoski [54] and Hakim [34] using discontinuous Galerkin algorithms (not shown in the figure).

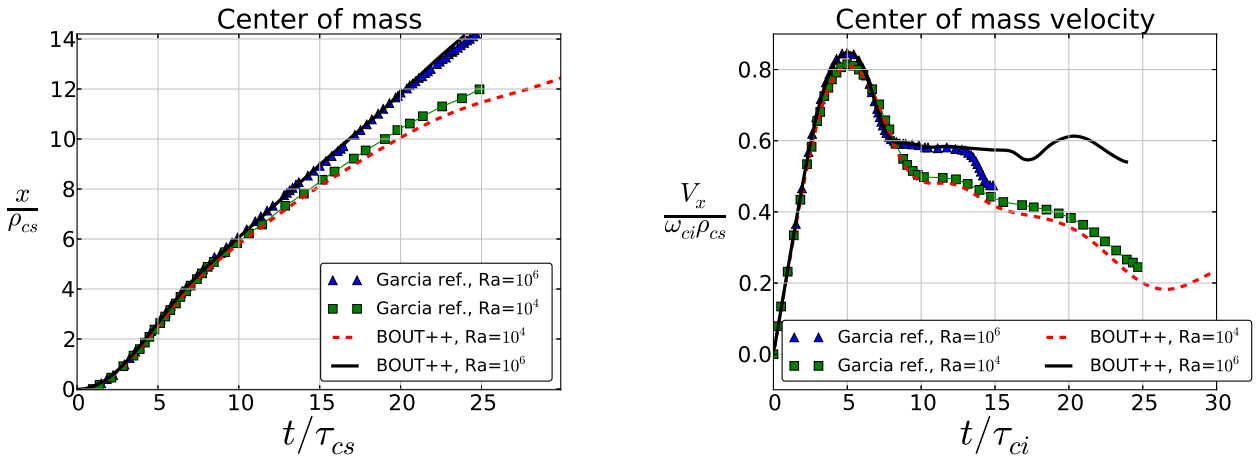

Figure 3.5: Comparison of blob trajectories calculated with BOUT++ to the results of E. Garcia [30], Two cases are compared corresponding to Rayleigh number 10^4 and 10^6.

3.2.3 Saturated turbulence

As an additional verification we examined flux-driven, many-blob interchange turbulence as described by Aydemir.[3] We used equation (3.2) as for single blob simulations, but with a nonzero density source term, S_n, and with radial boundary conditions that allow the profile to relax. Except for having a constant value of α, the simulation setup here is similar to ones described in section 3.3.2 of the present paper. Using $\beta/\alpha = 5$, we see excellent agreement of λ_{SOL} with the results present by Aydemir [3] across a wide range of parameters. Here as in [3], λ_{SOL} is determined by fitting a profile of the form $n = n_0 \exp(-x/\lambda_{SOL})$, to observed flux-surface averaged density values.

3.3 Numerical Studies of chaotic SOL

We now examine the effects of field-line chaos on SOL dynamics. We begin in Sec. 3.3.1 by describing the propagation of an isolated blob in a chaotic region. This motivates the investigation in Sec. 3.3.2 of the effect of chaos on saturated SOL turbulence. We then examine the modifications of the density profile in the SOL in Sec. 3.3.3 and the statistics of the associated fluctuations in 3.3.4.

3.3.1 Effect of field-line chaos on an isolated blob

In contrast to cases where α is a constant value or is simplified by averaging over flux-surfaces, blobs quickly lose coherence when propagating through a region with chaotic α as pictured in Fig. (3.6). This suggests that magnetic chaos may bring about significant changes in the properties of the SOL. The fine fractal structures of the Poincaré map, however, are not immediately apparent in the single blob response. In order to evaluate the impact field-line chaos has on the overall transport and the width of the SOL, it is clearly necessary to examine the saturated turbulent state with a distribution of self-consistently generated blobs.

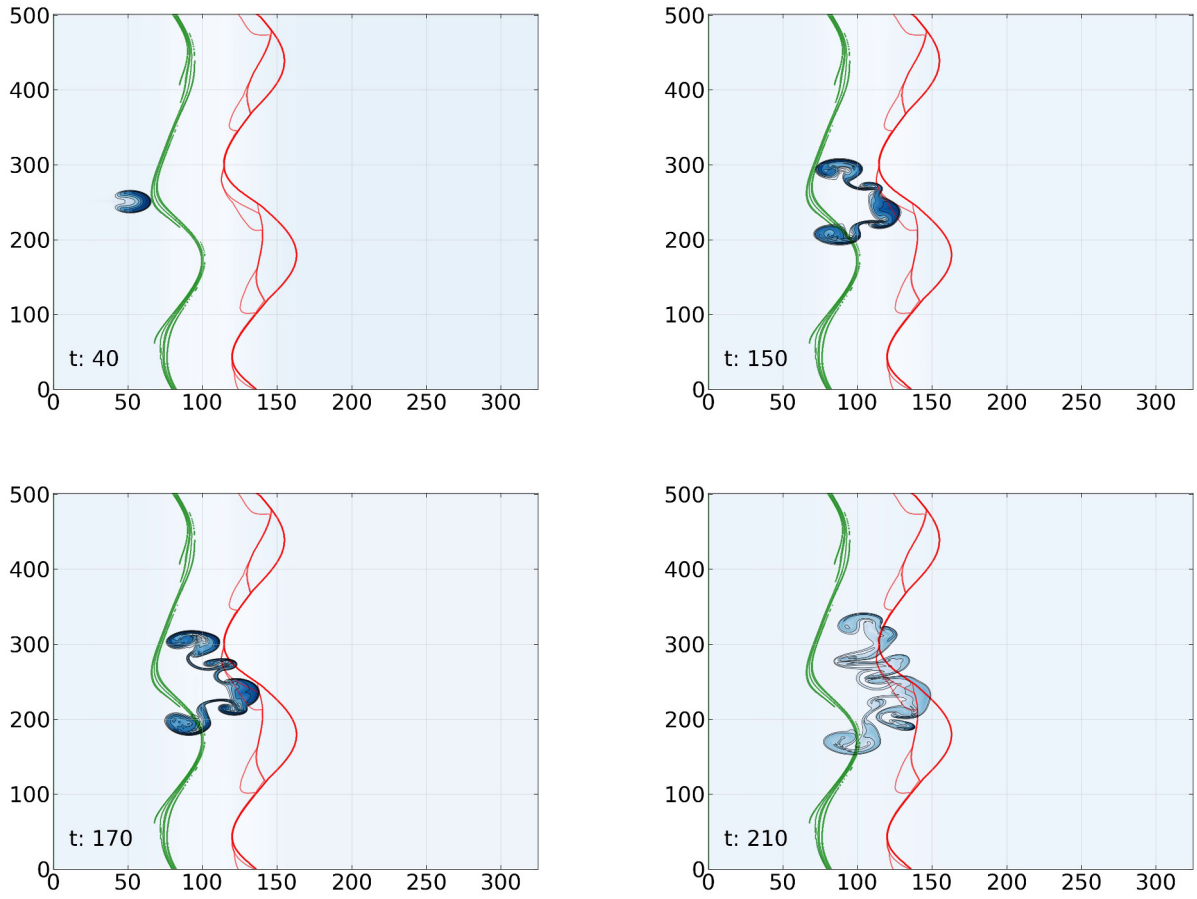

Figure 3.6: Evolution of a density blob across a region with chaotic magnetic fields for Rayleigh number = 10^4. The approximate extension of the chaotic region is shown here by the two equidistant curves. The structure quickly loses coherence as it propagates radially outward.

3.3.2 Effect of field-line chaos on saturated turbulence and mean blob size

In this section we are interested in examining the effect of field-line chaos on the SOL. Rather than focus on individual blobs we probe the changes in the mean blob be-

havior as we consider three scenarios: *a)* chaotic (Fig. 3.2), *b)* smooth (Fig. 3.3), and *c)* unperturbed flux surfaces.

The parameter space of parallel dissipation, diffusion, and source strength values is large and we opt to fix key parameters to be consistent with an NSTX tokamak configuration [67], with $\alpha_{max} = 3.0 \times 10^{-3}$, $\beta = 1.0 \times 10^{-2}$, $D_n = D_\varpi = 1.0 \times 10^{-2}$. Typical mesh size is $N_x \times N_y$ = 1024x512, the simulation domain represents a quarter of a full torus, and typical radial range is $L_x \approx 300\rho_s$. The large radial range, while not representative of the physical distance between the plasma and the wall, is useful in fitting density scaling parameters, see section 3.3.3. We see that the normalized inverse connection length, α, is similar to the mean α used in modeling a Helimak-like system shown in table ().

Simulations are initialized with a smooth density profile that gently peaks at the core-side edge and a small driving source term, S_n, as described in section (3.1.3). We use simple boundary conditions, $\partial_x n \approx 0$ and $u = 0$ on both radial boundaries, that allows the entire density profile to adjust as needed to settle on a turbulent equilibrium profile. Additionally we fix the potential, $\phi = 0$, on the inner radial boundary to ensure that the radial particle flux through the bounder vanishes so that the density is solely set by the balance between the source, S_n, and the sheath losses parametrized by α.

We can better interpret the many-blob turbulence results in terms of single blob theory by extracting mean blob behavior. To this end we consider fluctuations in the radial convective particle flux,

$$\Gamma_x = \Gamma_{E\times B,x}(x, y, t) = -n\partial_y\phi, \tag{3.10}$$

and employ spatial spectral analysis and radially resolved auto-correlation analysis to in-

fer the mean scale length of the saturated interchange turbulence present in our system. Specifically we considered the auto-correlation along the poloidal coordinate of the particle flux $\Gamma_x(x, y, t)$ at some fixed point x. We extract the mean periodic scale length and the smallest non-periodic statistically significant scale length, which we refer to as λ_{blob} and δ_{small} respectively.

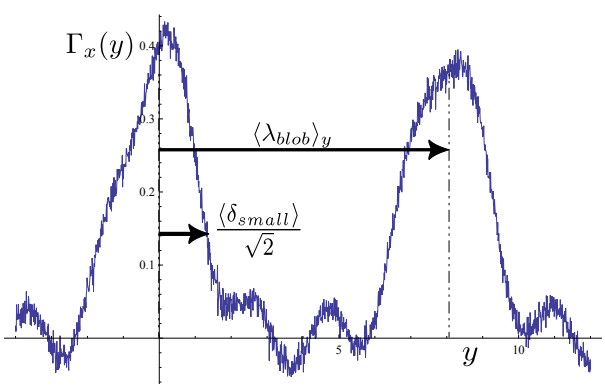

(a) A hypothetical $\Gamma_x(y)$ at a fixed x

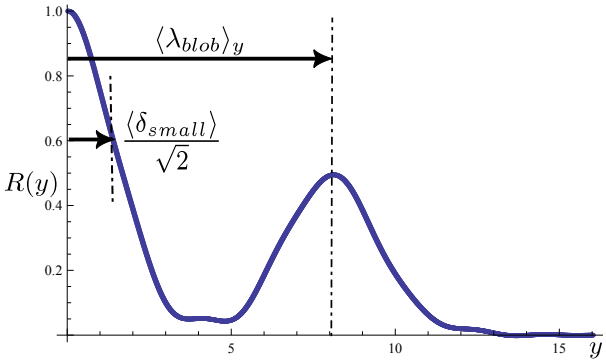

(b) Autocorrelation reveals the relevant length scales

Figure 3.7: The mean size of the smallest reoccurring feature in y can be shown to be $\langle\delta_{small}\rangle_y \approx \sqrt{2}\sigma$, where σ is determined by a least-squares fit of a Gaussian, $e^{-\frac{y^2}{2\sigma^2}}$, around the central peak of $R(y)$

When evaluating the flux Γ_x from the results of simulation, blobs will show up as isolated, generally radially outward propagating local maxima in $\Gamma_x - \langle\Gamma_x\rangle_y$. Consider Fig. (3.8), where a snapshot of the particle flux at a point in time is presented (3.8a), and more detailed figures follow, where $E \times B$ velocity fields are overlaid to give a sense of flow direction.

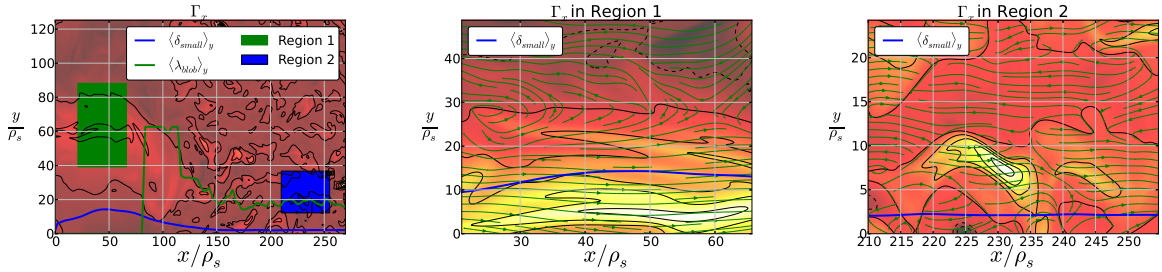

(a) snapshot of Γ_x

(b) Region 2 with $V_{E\times B}$ flow detail

(c) Region 1 with $V_{E\times B}$ flow detail

Figure 3.8: Details of radially outward particle flux Γ_x with average blob size $\langle \delta_{blob} \rangle_y$. The difference in the values of the α parameter is reflected in the size of the blobs in the two closeups images.

Parameter	Value
inertial lower limit:	$k_m = \frac{\sqrt{2}}{(\beta/\alpha^2)^{1/5}}$
diffusive upper limit:	$k_{D_n} = \frac{\sqrt{2}(\alpha D_n)}{\beta}$
parallel upper limit:	$k_\alpha = \frac{\sqrt{2}}{(\beta/\alpha^2)^{1/3}}$
viscous lower limit:	$k_{D_\omega} = \frac{\sqrt{2}}{(D_\omega/\alpha)^{1/4}}$
linear scale:	$k_{lin}(\gamma_{max}) \approx \left(\frac{\alpha}{D_n}\right)^{1/4}$
mean detected blob size:	$k_{\lambda_{blob}} \approx \frac{2\pi}{\lambda_{blob}}$
width of central peak of R_{Γ_x}:	$k_\sigma = \frac{\sqrt{2}}{\delta_{small}}$

Table 3.2: Wavenumber definitions

In Fig. (3.9) we superimpose the spectral density of fluctuations, analytic predictions, and scale lengths obtained from auto-correlation onto a single image that summarizes all important length scales as a function of x. The intensity of the filled contour plot is proportional to a time-averaged value of the spectral density. The spectral density is re-normalized at each radial location to clearly display the spectral density for all x,

even as the amplitude of fluctuations decays exponentially in the radially outward direction. See appendix (A) for additional details on auto-correlation analysis and background information on spectral density.

Wavenumbers associated with a few analytically predicted length scales are overlaid in Fig. (3.9). These expressions can be extracted from equation (3.2) using term balancing, see Aydemir.[3] As seen in Fig. (3.9) the blob size, for the parameters considered, stays close to the inertial scale length, and the mean size of the finer structures, δ_{small}, stays close to the most unstable linear scale. The inertial scale is the length scale at which both inertia and parallel momentum losses are comparable with the curvature drive. Relating operators in the momentum equation (3.2a) to some typical blob size a we may write the various terms of this equation symbolically as

$$\left(\frac{\phi}{a^2}\right)^2 + \frac{\beta}{a} - \alpha\phi + \frac{D_\omega \phi}{a^4} = 0, \tag{3.10}$$

the desired length scale a_m follows by balancing the curvature term against the inertia and the sheath-loss:

$$\left(\frac{\phi}{a_m^2}\right)^2 \approx \frac{\beta}{a_m}, \qquad \alpha\phi \approx \frac{\beta}{a_m}. \tag{3.10}$$

It follows easily that equation (3.3.2) is satisfied when

$$a_m^5 = \beta/\alpha^2. \tag{3.10}$$

Examining Fig. (3.9) further, we observe that the spectral density appears to taper off below the parallel upper limit k_α. Modes below this value are dominated by end-losses, and typically lose mass and lose coherence quickly. We can derive this length scale

similarly to the preceding example. Rewriting operators in the continuity equation in terms of the scale length a yields

$$\frac{D_n}{a^2} + \frac{\phi}{a^2} + \alpha = 0. \tag{3.10}$$

When parallel particle losses roughly balance particle flux in equation (3.3.2), and curvature drive is comparable to parallel momentum losses in equation (3.3.2) the implied length scale a_α must satisfy

$$\frac{\phi}{a_\alpha^2} + \alpha \approx 0 \qquad\qquad \alpha\phi \approx \frac{\beta}{a_\alpha}, \tag{3.10}$$

from which it follows that

$$a_\alpha^3 = \beta/\alpha^2. \tag{3.10}$$

We also note that the curvature-drive term gets bigger as a gets smaller, therefore a_α must be the smallest length scale at which parallel dissipation can be comparable to curvature drive. In k-space this will correspond to some upper wavenumber limit, where $k_\alpha = \sqrt{2}/a_\alpha$, when we correctly relate periodic and spatially localized/non-periodic length scales. As an aside, we observe that in order to correctly associate a non-periodic or spatially localized length scale with a wavenumber we use the auto-correlation function of the two signal types. Consider an auto-correlation function of a sine wave, and an auto-correlation function of some non-periodic signal, call them R_{sine} and $R_{noperiod}$ respectively. As reviewed in figure(3.7) the central peak of the auto-correlation function $R_{noperiod}$ will have a standard deviation of $\sqrt{2}\sigma_x$, where $2\sigma_x$ can be equated with a diameter a. The auto-correlation of a periodic signal will be another periodic signal with the same period as the input signal. Using least-squares we can fit a

Gaussian around the central peak of R_{sine} to see that it has a standard deviation of $1/k$. It follows that $1/k = \sqrt{2}\sigma_x = \sqrt{2}a/2 \Rightarrow k = \sqrt{2}/a$.

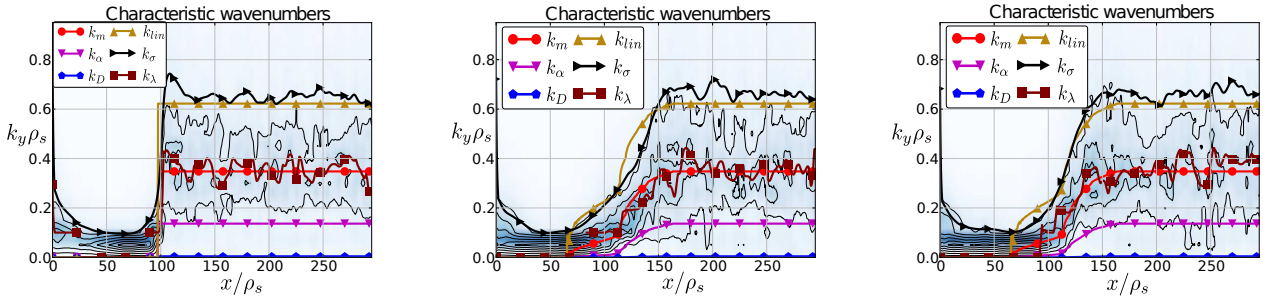

(a) unperturbed α (b) chaotic α (c) smooth α

Parameter	Value
inertial lower limit:	$k_m = \frac{\sqrt{2}}{(\beta/\alpha^2)^{1/5}}$
diffusive upper limit:	$k_{D_n} = \frac{\sqrt{2}(\alpha D_n)}{\beta}$
parallel upper limit:	$k_\alpha = \frac{\sqrt{2}}{(\beta/\alpha^2)^{1/3}}$
viscous lower limit:	$k_{D_\omega} = \frac{\sqrt{2}}{(D_\omega/\alpha)^{1/4}}$
linear scale:	$k_{lin}(\gamma_{max}) \approx \left(\frac{\alpha}{D_n}\right)^{1/4}$
mean detected blob size:	$k_{\lambda_{blob}} \approx \frac{2\pi}{\lambda_{blob}}$
width of central peak of R_{Γ_x}:	$k_\sigma = \frac{\sqrt{2}}{\delta_{small}}$

Figure 3.9: Wavenumbers or length scales present in Γ_x fluctuations indicate that the inertial scale length, with a corresponding wavenumber k_m, provides a good estimate of the mean blob size. Additionally we observe that the smallest significant scale length corresponds to a length scale for which we expect the linear growth rate γ to peak, where $k = k_{lin} \approx (\alpha/D_n)^{1/4}$. The nature of the abrupt jump in α field is clear in Fig. (a). The differences between smooth (Fig. 3.3) and chaotic (Fig. 3.2) cases, however, is more modest. As indicated by the black curve, significant blob break-up is observed in all three cases.

Fig. 3.9(a) shows that in the unperturbed equilibrium, the SOL turbulence is well-localized outside the separatrix, whereas Fig. 3.9(b) shows that in the presence of chaos

the turbulent spectrum spreads smoothly as one traverses the chaotic layer. In the laminar region outside of the chaotic layer, $x/\rho_s > 160$, the spectra for the unperturbed, chaotic, and smoothed-α cases are indistinguishable: the dominant blob size adjusts rapidly to the prevailing α. Comparison of the chaotic and smoothed spectra in the region $75 < x/\rho_s < 160$ in Figs. 3.9 (b) and (c) shows that the mean blob size does not seem to be strongly affected by the fractal character of the α field but does seem to respond quickly to the local-in-x variations in the y-averaged parallel connection length, as indicated by the curve labeled k_λ. We expect the smallest observed, δ_{small}-sized, fluctuation and its corresponding wavenumber k_σ to be most sensitive to the chaotic nature of the field-lines. While generally k_σ closely tracks the most unstable linear wavenumber, $k_{lin} \approx (\alpha/D_n)^{(1/4)}$, in the region where α transitions from 0 to α_{max} the k_σ wavenumber seems to be consistently smaller in the case with chaotic field-lines than in the case with the smooth simplification pictured in Fig. 3.9(c). The simplest explanation for this observed difference is that highly spatially localized variations in α, associated with fast escape times, are essentially ignored by the smallest coherent flux structures, lowering the effective average value of α which determines the unstable linear scale length. In relation to the Poincaré magnetic field-line map this observation implies that highly localized escape basins, while allowing individual particles to escape toroidal confinement quickly, do not qualitatively change the character of the average radially propagating coherent structure.

We have seen that the mean blob size does not seem to be strongly affected by the fractal character of the α field but does seem to respond quickly to the local-in-x variations in the y-averaged parallel connection length. For many machines inertial blobs can be expected to be several multiples of the ion-acoustic gyro-radius,

$$a_m = (\frac{(2\pi q(R))^2 R}{\rho_s})^{1/5}\rho_s \approx (2-3)\rho_s. \tag{3.10}$$

Note that the simple approach taken above to arrive at a set of characteristic length scales on the non-vanishing α end of the simulation domain neglects zonal flows which are seen to dominate the $\alpha = 0$ end of the simulation domain, and are in fact present throughout. Zonal flows are important in setting the blob creation rate and have a non-trivial interaction with radial electric field shear.[67]

One expects the above differences between unperturbed and chaotic SOL dynamics to have an influence on the profile of density in the SOL. To characterize this influence, we next examine ways of modeling this profile that enable the effect of the chaos to be quantified.

3.3.3 Profile characterization

In order to describe the effect of chaos on the density profile, we fit a simple profile to our simulation results where the gradient of $\log(n_{\text{fit}})$ along x smoothly changes from some λ_{core} to another λ_{SOL} with some transition region of width w_n linking inner and outer regions,

$$\partial_x \log(n) = A + B \arctan\left(\frac{x - x_0}{\Delta x}\right) = 0, \tag{3.11}$$

$$A = \frac{\lambda_{core} + \lambda_{SOL}}{2}, \tag{3.11}$$

$$B = \frac{\lambda_{SOL} - \lambda_{core}}{\pi}. \tag{3.11}$$

Integrating equation(3.11) yields a longer analytic expression and introduces a constant of integration. We minimize the difference of the squares to compute $\Delta x, \lambda_{SOL}, \lambda_{core}$ and the constant of integration. We find a region of width w_n where the derivative of n_{ave} is within one standard deviation of maximum value. This w_n is the value reported on the y-axis in Figure(3.11).

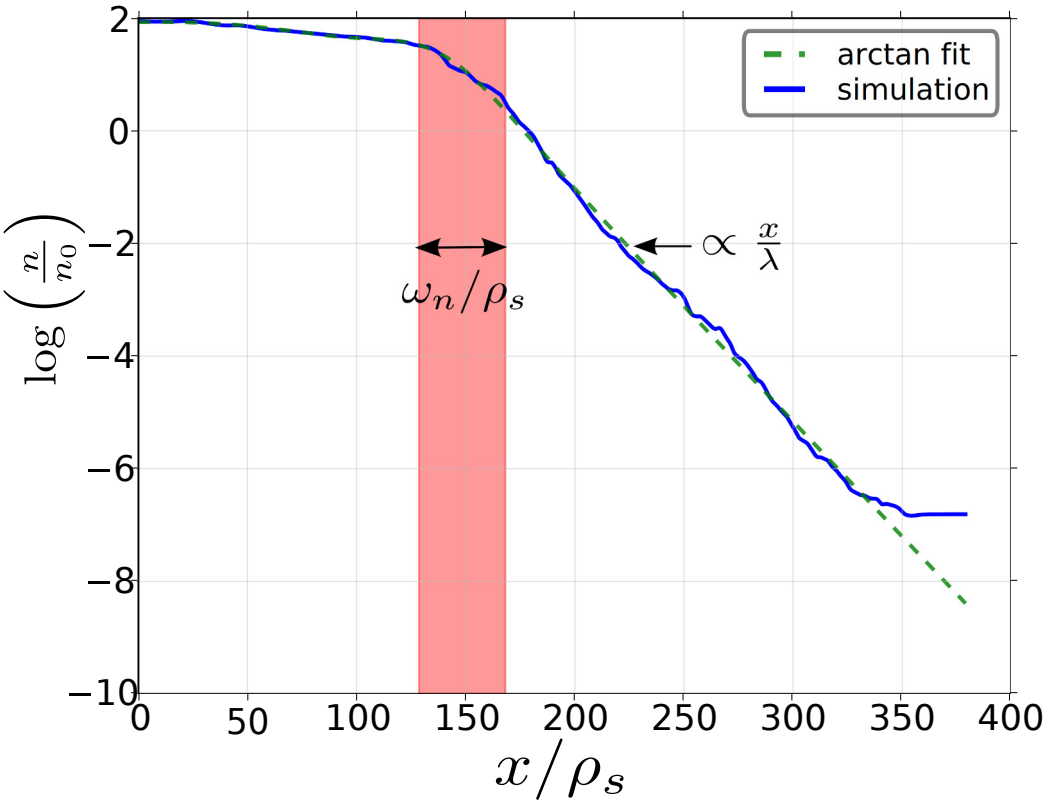

Figure 3.10: Typical n_{ave} profile (solid) with the detected shoulder region shaded, along with a fit of a smoothly connected two-λ profile model (dashed).

The width of the density shoulder, w_n, appears to scale linearly with the width of the α-transition, w_α, irrespective of whether chaotic (Fig. 3.2) or smooth (Fig. 3.3). The

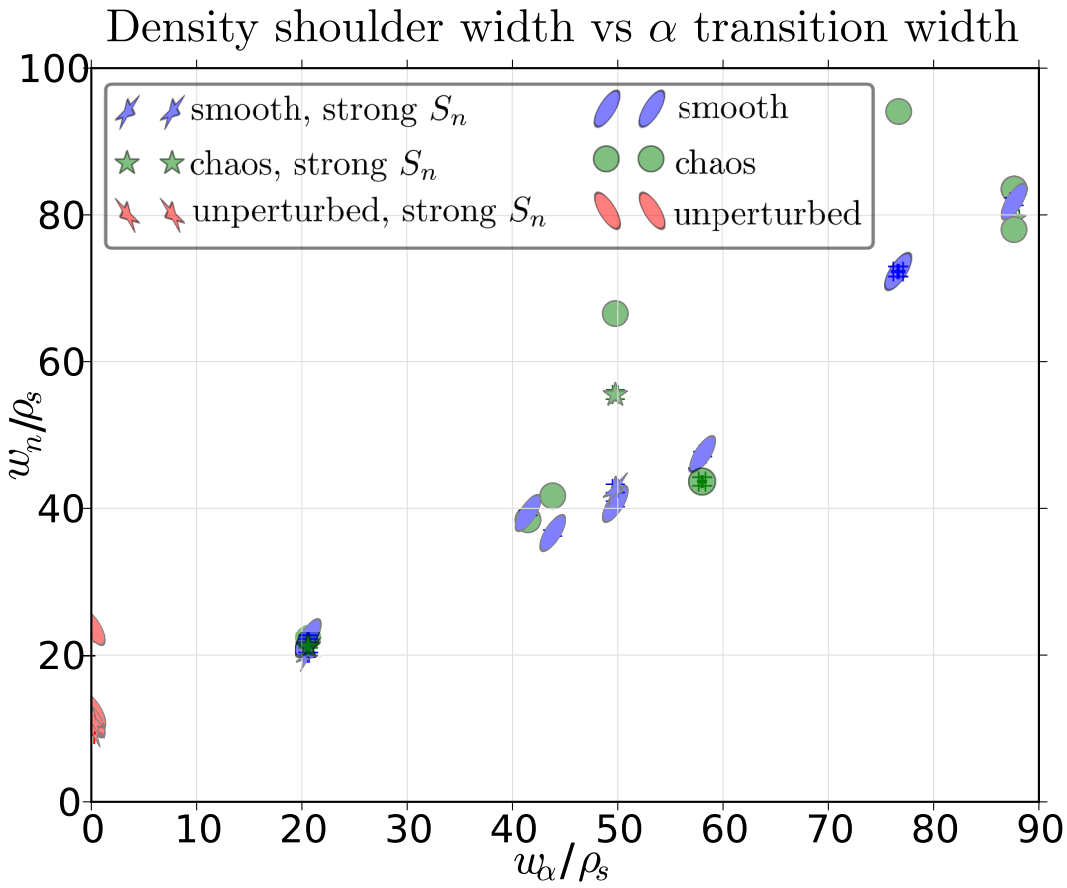

Figure 3.11: Dependence of the transition width in the density profile ('shoulder') on the width of the transition in the α profile. While for the chaotic cases we see a greater number of large deviations from a simple linear relationship between the width of the α mixing length and the width of the n_{ave} shoulder, the linear relationship seems to lie within the same scaling range as the smooth α set of values.

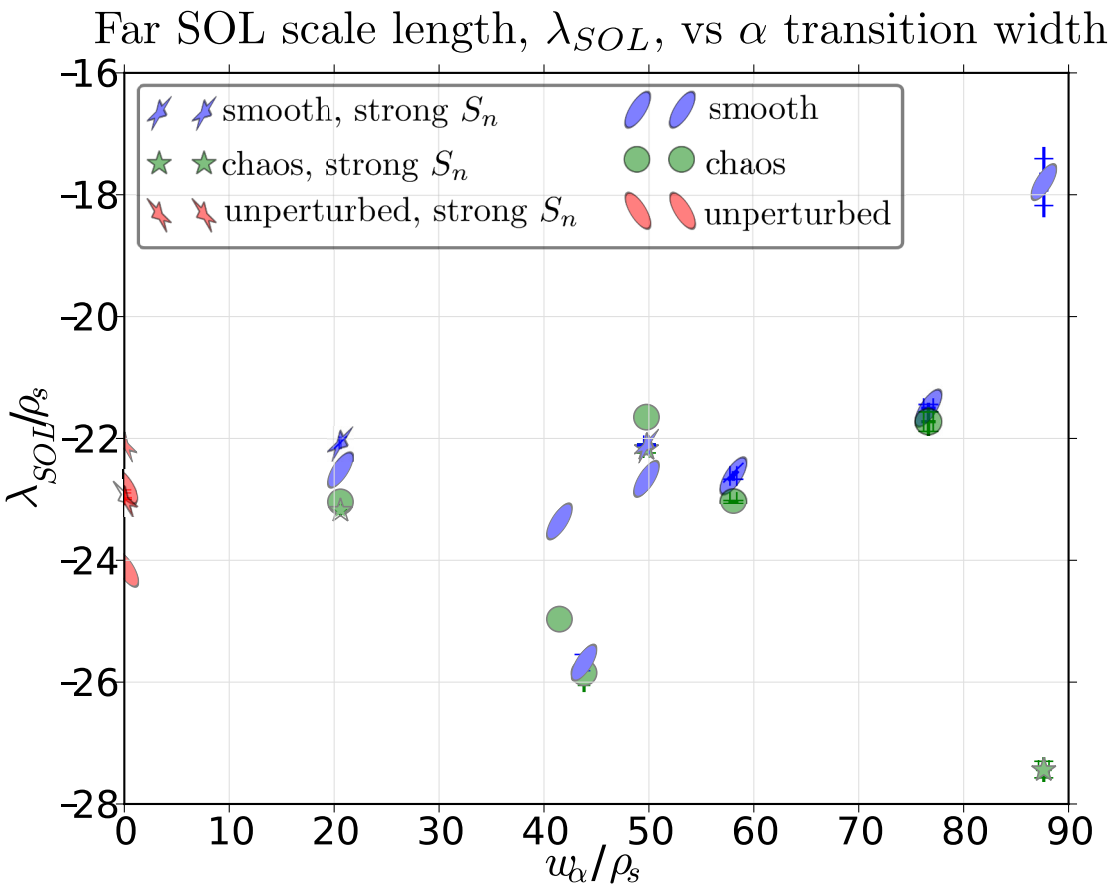

Figure 3.12: The width of the far SOL, λ, does not show any clear dependence on the chaotic properties of the α profile

density scale length λ_{SOL} in the far SOL, by contrast,displays no clear dependence on the character of the α transition. This observation, combined with blob size measurements in section (3.3.2), indicates that both globally averaged profiles and the mean blob-size are consistently insensitive to the finer details of how α transitions from 0 to some maximum α_{max}. In the next section, rather than simply compute the average profiles and blobs sizes, we examine the distribution of fluctuations in greater detail. Aydemir [3] has proposed modeling transport in the SOL with a collection of blobs, sized at roughly the most unstable linear scale length at birth that propagate radially outward. Our observations are consistent with this approach and explicitly verify that inertial blobs dominate convective particle flux fluctuations.

While resolving the large spatial variations in α along the poloidial dimension as opposed to approximating with an average value does not seem to strongly influence the mean blob size or the mean profile shape these measures are partially meant to help us understand how RMPs change the incident particle flux on the divertor, which can also examine directly from $\langle \alpha n \rangle_{flux\ surf.}$. What we see is that regardless of the level of poloidal details retained in α, the application of RMPs does change the mean profile and perhaps the most importantly for divertor erosion greatly reduces the maximum of the incident particle flux on the divertor. Specifically as illustrated in figure 3.13 the flux-surface average value of parallel flux is reduced by a factor 3.5 when RMPs are applied.

3.3.4 Statistics of density and convective flux fluctuations in the SOL

Single point measurements of density fluctuations are possibly the most common way to detect large bursty events in the SOL and a large body of experimental and theo-

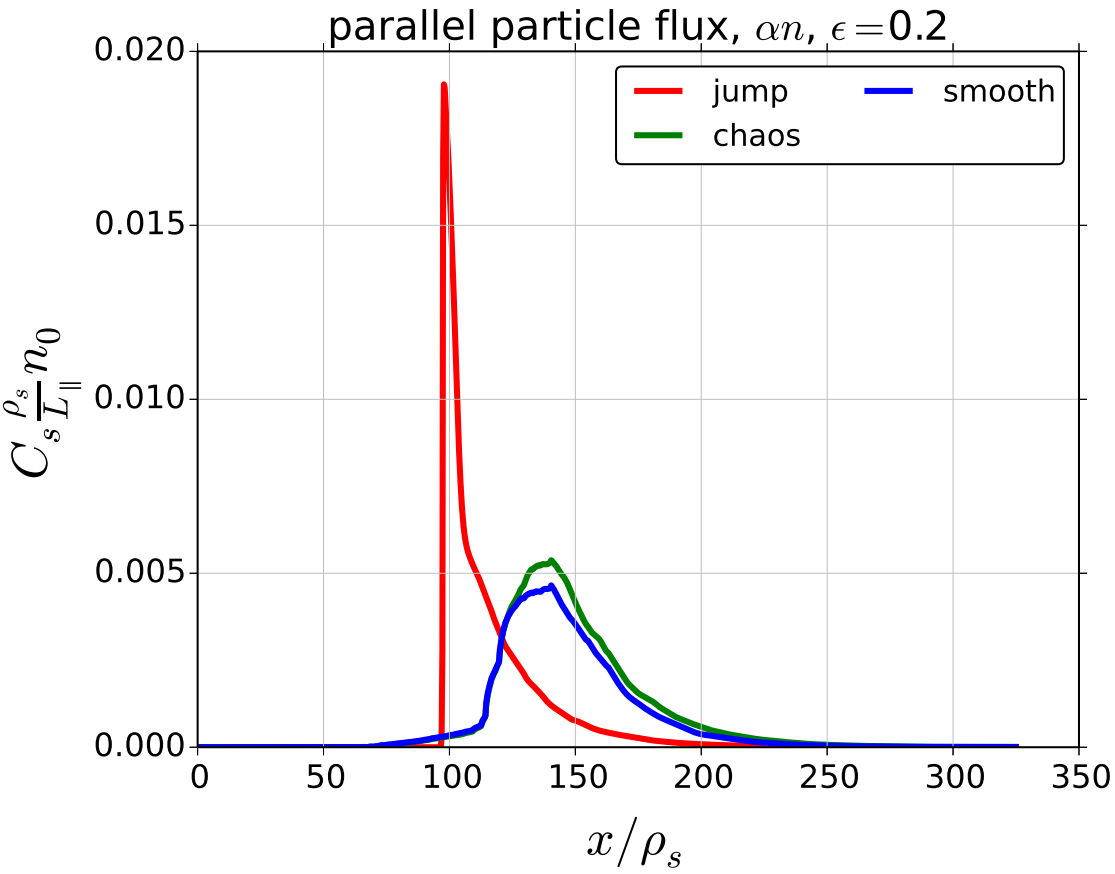

Figure 3.13: The parallel particle flux incident on the divertor is greatly reduced with RMP application. Both fully chaotic and flux-surface averaged models produce a similar reduction

retical work surrounds this diagnostic in the context of blobs and many-blob turbulence [29, 87, 45]. One difference between data-gathering permitted by numerical work over experiment is that rather than being limited to several locations where probe data is available we can consider fluctuations across the entire computational domain. Additionally we can consider fluctuations in the radial component of the particle flux, Γ_x. This is a simple way to limit our attention to density fluctuations that have a nonzero radial velocity component. To examine how different distributions deviate from an idealized Gaussian we can normalize the bins enumerating the number of counts of a particular flux amplitude with the Γ_{rms} specific to that numerical experiment. With this approach all Gaussian distributions, regardless of their individual Γ_{rms} values would sit on a single curve.

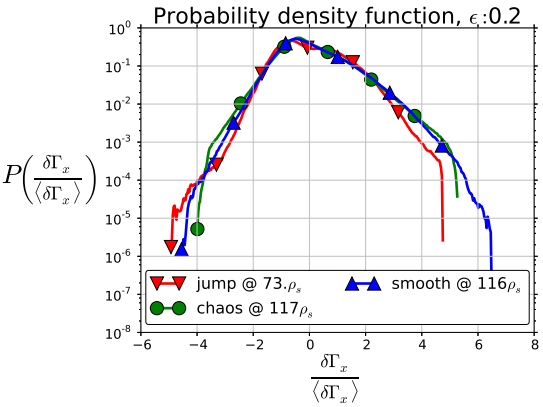

(a) Histogram of normalized convective particle flux Γ_x fluctuations. The manner in which chaotic and smooth α distributions deviate from a Gaussian is similar.

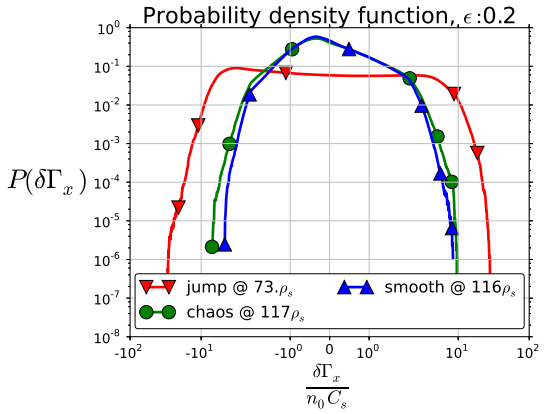

(b) Histogram of unnormalized Γ_x fluctuations. We see the unperturbed case has a strongly bimodal distribution and largest absolute deviations from its mean value.

Figure 3.14: Histogram of (a)normalized and (b)unnormalized fluctuations in the convective particle flux Γ_x near the maximum in the density gradient (in practice this is usually just outside the separatrix). The chaotic and smoothed cases correspond to a magnetic perturbation with $I_{ext}/I_p = .2$. As seen in panel (b), the precise distribution of the of the chaotic α has little effect on the frequency of high flux events as compared to the smooth case.

Figure 3.14 shows two histograms for normalized and unnormalized fluctuations in the convective particle flux Γ_x near the maximum in the density gradient, i.e. at the separatrix for the unperturbed case and in the chaotic region for the perturbed case (Fig. 3.2) and the smoothed-α model (Fig. 3.3). Fig. 3.14(a) shows that the manner in which chaotic and smooth α distributions deviate from a Gaussian is similar. Fig. 3.14(b) confirms the similarity of the smoothed-α model with the chaotic case, and further reveals that the unperturbed case has a strongly bimodal distribution and the largest absolute deviations

from its mean value.

Looking beyond the shoulder region to the laminar region where the field-line length (and thus the sheath-loss coefficient α) is independent of the presence of a perturbation, Fig. 3.15(a) shows that all three cases appear to have a very similar distribution of fluctuations. In Fig. 3.15(b), the significantly lower values of flux fluctuation for the unperturbed case (abruptly changing α) can be understood by noticing that for a given position outside the separatrix, the density field has experienced more parallel dissipation as it moved radially outward, due to lack of intermediate values of α between 0 and α_{max}.

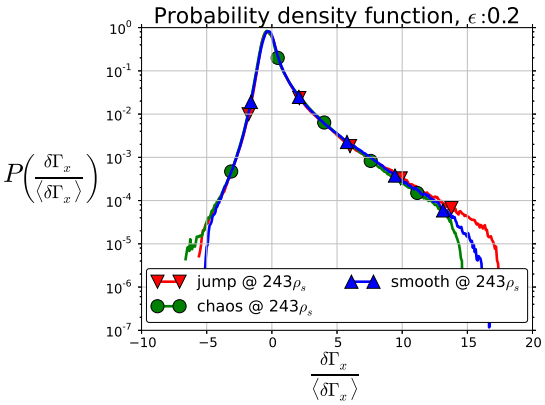

(a) Histogram of normalized convective particle flux Γ_x fluctuations. The three distributions appear essentially the same far enough from the separatrix.

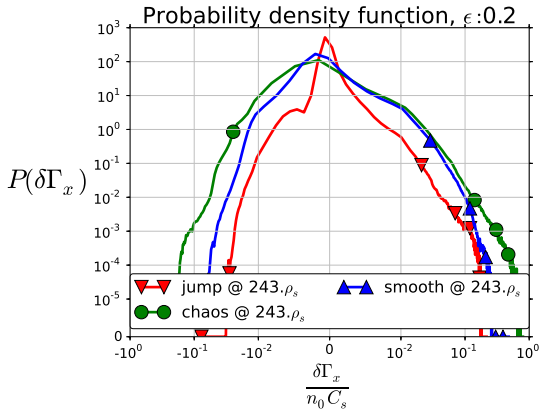

(b) Histogram of unnormalized Γ_x fluctuations. The significantly lower values of flux fluctuation for the abruptly changing α can be reconciled by noticing, that for a given position outside the separatrix, the density field has experienced more parallel dissipation as it moved radially outward, due to lack of intermediate values of α between 0 and α_{max}.

Figure 3.15: Histogram of (a) normalized and (b) unnormalized fluctuations in the convective particle flux Γ_x far from the separatrix.

The histograms of density fluctuations shown in Fig. 3.16 tell a similar story, with little difference in either the overall shape of the fluctuation distribution or maximum values of particle flux between the chaotic α case and the smoothed-α model. The unperturbed case, by contrast, (abruptly changing α), displays a significantly different distribution that is strongly bi-modal and exhibits a greater number of high intensity events. This observation is qualitatively consistent with section (3.3.2) where we note that immediately outside the separatrix for the unperturbed case, the observed blobs, as inferred from auto-correlation of Γ_x, are smaller and therefore can be expected to travel faster and

generate sharper wave-fronts [9] relative to larger blobs. Whatever initial differences may have been observed between the three distributions immediately outside the separatrix mostly disappear when the point of observation moves $1/2$ of the total radial domain size away from the separatrix, as pictured in Fig. (3.15).

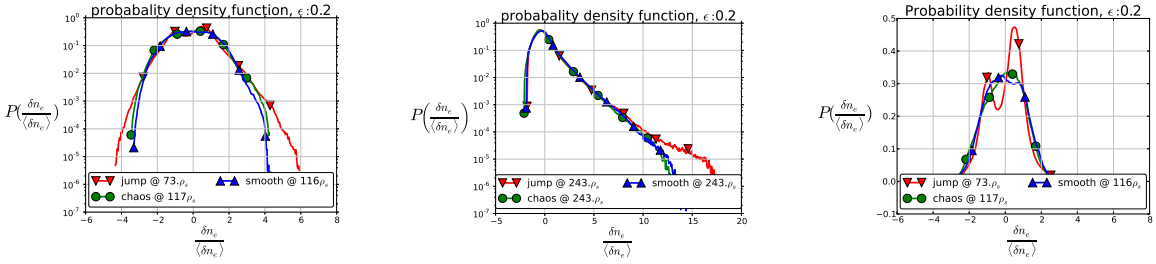

Figure 3.16: (a) Probability density function (PDF) of density fluctuations near the peak density gradient show that the case with an unperturbed α, in red, has the highest relative number of high density events. When fluctuation counts are normalized, the differences between smoothly varying and chaotic α fields are small and subtle. Only the $\epsilon = .2$ case is illustrated here, however other values of ϵ yield qualitatively similar results. (b) Probability density function (PDF) of density fluctuations outside of the chaotic region. Here the probability distributions collapse onto a single curve characterized by some positive skewness, indicative of intermittent positive density events. (c) Again near the peak density gradient linear y-axis scaling reveals that the case with an unperturbed α, in red, has the most clearly bimodal (two-peak) distribution among the considered cases, indicating a region where blobs and holes tend to have a relatively narrow range of typical density values, respectively, as compared to the other cases.

We note that fluctiations in divetor incident parallel particle flux are simply density fluctuations rescaled with α. With this interpretation in mind we see from figure (3.16) that RMP generated α fields, both fully chaotic and flux-surface averaged versions, lower the maximum divertor incident flux. As evidenced in figure (3.14) the absolute value of radial particle flux fluctuations is similargly damped when RMPs are applied.

A quantitative treatment examining skewness and kurtosis, the leading moments of the density PDF beyond the simple mean and standard deviation, can be used to further quantify intermittency and identify the blob birth zones. This analysis, however, reveals little systematic difference between chaotic and smooth α fields.

3.4 Conclusion

Using a simple, 2D edge-turbulence model applicable to a broad range of devices, we have shown that magnetic chaos created by RMP broadens the steady-state density profiles in turbulent SOL. In the far scrape-off layer (outside of the chaotic region), the characterization of the SOL density by the common metric of an e-folding length remains largely unchanged. Closer to the separatrix however, in the region where chaos causes the sheath-loss parameter α to transition between $\alpha = 0$ and α_{max}, the mean density profile has an inflection point and a local maximum in the density gradient. The width w_n of the peak in the density gradient is proportional to the width of the chaotic region, w_α. The broadening is insensitive to the details of the field-line chaos and we observe almost identical properties when replacing the chaotic sheath-loss parameter by its average along the unperturbed magnetic surfaces.

We observe that radial transport in this SOL model is dominated by blobs of a specific size, regardless of the nature of the interface between the closed flux surfaces and the far SOL. Furthermore, the observed density scale-length is only weakly affected by the state of the plasma at the interface where blob birth takes place, once a sheath-connected blob is established. While the introduction of a chaotic interface, where externally introduced magnetic field deforms or even breaks the last closed flux surface, does encourage

blob and hole formation over a wider radial region, the same effect can be modeled by running the numerical experiment with smoothly varying connection lengths lacking any chaotic features.

Ideally, a 2D simulation of magnetic field line chaos would include highly localized parallel transport effects that strongly couple physical observables between a set of points intersected by the same field-line. Specifically we expect parallel current to short points, that may be well displaced in the perpendicular plane, but are in fact neighbors along a chaotic field line. The equilibrium sheath potential would then be determined by both sheath physics as well as other parallel transport channels. Parallel currents facilitated by magnetic chaos have the potential to disrupt the coherent potential dipole structures essential to radial blob propagation in this study. The most straightforward solution to this geometric issue is to include the parallel dimension in the simulation domain rather than develop non-local computational techniques in the perpendicular plane.

Our calculations of probability density functions (PDFs) for the observed density and convective radial flux fluctuations show that a chaotic magnetic field will generally produce fluctuation statistics that differ insignificantly from the smoothly varying case. This again suggest that assuming a smoothly varying parallel connection length between just inside separatrix and the far SOL is a sufficient description when dealing with physics that is otherwise well characterized by a simple 2D electrostatic model. Additionally, as seen in Fig. 3.14 as well as Fig. 3.13, the application of chaotic magnetic fields does in fact lower the maximum radial convective and mean parallel particle fluxes that can be expected, suggesting that RMPs may be helpful in limiting divertor damage and impurity contamination.

Our results are consistent with experiments on MAST in double-null L-mode discharges [72]. These experiments showed only a small reduction in SOL particle-transport during application of the error-field correction coil (ECC) of amplitude such as to create magnetic chaos in the absence of plasma response. The MAST observations and our own results, however, differ from observations on TORE-Supra [16] and TEXTOR [85] that found large reductions in the size and velocity of blobs and thus in the turbulent radial flux in the SOL. A possible explanation for this is that in these two machines, neither of which had an X-point, the application of resonant perturbations led to a significant decrease in the electron temperature in the SOL.[72] This explanation is undermined, however, by the 3D simulations of Reiser showing that a constant temperature model can reproduce the stabilizing effect of an RMP.[64] Those simulations displayed flattening around the X-points of the RMP-induced islands, suggesting that parallel transport may be responsible for the changes to the SOL turbulence. In particular, parallel transport caused by RMPs reduces the flux that has to be carried by blob filaments. In the 2D model used here, however, reducing the driving flux does not affect the size or velocity of the blobs, so that we cannot account for the observations in the circular machines by invoking the diversion of flux by parallel transport. The flattening around the X-point could also be understood in terms of localized enhancement of cross-field diffusion, which we did not account for in this work, but would be implicitly present in a 3D simulation with parallel transport effects. Additionally if the dominant mechanism by which experimentally realizable RMPs disrupt blob creation and propagation is by shorting out the potential dipole structure, responsible for radial blob propagation, rather than by creating a chaotic α field, this important physical mechanism, missing from our current model, may

be in part responsible for incomplete agreement with experiment. More work experimental and theoretical work is clearly needed to clarify the circumstances when RMP reduce intermittency in the SOL.

Appendices

Appendix A

Autocorrelation

We consider the auto-correlation along the poloidal coordinate of the particle flux $\Gamma_x(x, y, t)$, at some fixed point x. We define the auto-correlation as the usual measure of similarity of a signal with itself shifted by some poloidal displacement,

As shown in Fig. (3.7) at least two characteristic length scales can be extracted: the width of the central peak of R, referred to as $\langle\delta\rangle_y$ and some primary period $\langle\lambda_{blob}\rangle_y$, or in shorthand notation δ_{small} and λ_{blob}. We anticipate that λ_{blob} is a wavelength that can be related to mean blob size, and δ_{small} is simply the smallest observed coherent convective density flux structure that is statistically significant. In the subsequent discussion we show that δ_{small} and λ_{blob} agree well with simple analytic predictions of dominant linear instability scale length and blob size, respectively.

In addition to computing the auto-correlations of Γ_x, we can consider a discrete Fourier transform of Γ_x, specifically

$$\widetilde{\Gamma}_x = \widetilde{\Gamma}_x(x, k_y, t) = \int_0^{L_y} dy\, e^{-i2\pi k_y y}\, \Gamma_x. \tag{A.0}$$

We can go on to compute a time average of the spectral density $P(x, k_y, t)$, where

$$P(x, k_y) = \overline{P(x, k_y, t)} = \frac{1}{(t_1 - t_0)} \int_{t_0}^{t_1} dt\, \widetilde{\Gamma}_x \widetilde{\Gamma}_x^{\star}. \tag{A.0}$$

Note that this is simply the absolute value of the Fourier transform $\widetilde{\Gamma}_x$, squared and time averaged, or equivalently a Fourier transform of the auto-correlation $R(x, k_y)$ time averaged. Local maxima of $P(x, k_y)$ along k_y indicate dominant wavenumbers; important periodic features along the poloidal direction.

Appendix B

Extracting phase and growth rates

Given some system response $A(x_n, t)$ We can consider consider a Fourier space representation.

$$\tilde{A}_k(t) = \sum_n A(x_n, t) e^{-i2\pi kn/N} \tag{B.0}$$

$$A(x_n, t) = \frac{1}{N} \sum_k \tilde{A}_k(t) e^{i2\pi kn/N} = \frac{1}{N} \sum_k A_k(t) e^{i\phi_k} e^{i2\pi kn/N} \tag{B.0}$$

For a linear system the response can be represented by a linear combination of several frequencies for any given $\vec{k}$, as usual the relationship between $\tilde{\omega}$ and k can be established by substituting this form of the solution back into the linearized equations evolving the system.

$$A(x_n, t) = \frac{1}{N} \sum_{k,\tilde{\omega}} A_{k,\tilde{\omega}} e^{i2\pi kn/N} e^{i\tilde{\omega}t} \tag{B.0}$$

In practice k is a discreet vector, and $\tilde{\omega}$ is complex.

$$k = \vec{k} = 3\frac{2\pi n_x}{L_x}\frac{2\pi n_y}{L_y}\frac{2\pi n_z}{L_z} \tag{B.0}$$

We can identify relevant modes by considering the power profile at any given point in time or by selecting them at will as needed, especially if we want to measure the growth rate,γ, for a damped or otherwise not dominant modes.

$$P(t)_k = \tilde{A}_k(t)\tilde{A}_k(t)^\star \tag{B.0}$$

We can extract phase and amplitude associated with any given k vector. Numerically integrating the system for any significant period of time will effectively filter all but the fastest growing mode for any given k. Define $\tilde{\Omega}$

$$\tilde{\Omega} = \omega + i\gamma_{max} \tag{B.0}$$

$$A(x_n, t) = \sum_{k,\tilde{\omega}} A_{k,\tilde{\omega}} e^{i2\pi kn/N} e^{i\tilde{\omega}t} \rightarrow \frac{1}{N} \sum_{k} A_{k,\Omega} e^{i2\pi kn/N} e^{i\tilde{\Omega}t} \tag{B.0}$$

So given sufficient integration time the Fourier coefficient only reflects the dominant mode for any given k.

$$\tilde{A}_k(t) = A_k e^{i\tilde{\Omega}t + \phi_0} \tag{B.0}$$

Having computed $\tilde{A}_k(t)$, for a single fixed k consider $\frac{A_k(t+\Delta t)}{A_k(t)}$

$$\frac{\tilde{A}_k(t+\Delta t)}{\tilde{A}_k(t)} = \frac{e^{i\tilde{\Omega}_k t + i\tilde{\Omega}_k \Delta t}}{e^{i\tilde{\Omega}_k t}} = e^{i\tilde{\Omega}_k \Delta t} \tag{B.1}$$

$$\tilde{\Omega}_k = -i\frac{d}{dt} \ln(\tilde{A}_k(t)) = -\frac{i}{\Delta t} \ln\left(\frac{\tilde{A}_k(t+\Delta t)}{\tilde{A}_k(t)}\right) \tag{B.1}$$

B.0.0.1 Uncertainty Estimation

To estimate the uncertainty we propagate the absolute tolerance of the field using the chain rule. We approximate $\delta A_k(t) \approx \delta A_k(t + \Delta t)$

$$\delta\tilde{\omega}_k = -\frac{i}{\Delta t}\left(\frac{\tilde{A}_k(t)}{\tilde{A}_k(t+\Delta t)} \delta\left(\frac{\tilde{A}_k(t+\Delta t)}{\tilde{A}_k(t)}\right)\right) \tag{B.2}$$

$$\delta\tilde{\omega}_k = -\frac{i}{\Delta t}\left(\frac{\delta\tilde{A}_k(t+1)}{\tilde{A}_k(t)} + \frac{\delta\tilde{A}_k(t)}{\tilde{A}_k(t+1)}\right) \approx -\frac{2i}{\Delta t}\frac{\delta\tilde{A}_k(t)}{\tilde{A}_k(t)} \tag{B.2}$$

If we estimate the uncertainty of the field $A(x_n, t)$ as Gaussian white noise we can show

$$\delta A_{x,t} = |\widetilde{\delta A_{k,t}}| \tag{B.3}$$

$$\widetilde{\delta A_{k,t}} = \frac{1+i}{\sqrt{2}} |\widetilde{\delta A_{k,t}}| \tag{B.3}$$

Putting everything together

$$\delta\omega = \delta\gamma = \frac{\sqrt{2}}{\Delta t}\frac{\delta A}{A} \tag{B.3}$$

We can identify $\frac{\delta A}{A}$ as the relative tolerance of the system. Typically this quantity is on the order of 10^{-7} for cases considered in this work.

Bibliography

[1] Justin R. Angus, Sergei I. Krasheninnikov, and Maxim V. Umansky. Effects of parallel electron dynamics on plasma blob transport. *Physics of Plasmas*, 19(8):082312, Aug 2012.

[2] Justin R. Angus, Maxim V. Umansky, and Sergei I. Krasheninnikov. Effect of Drift Waves on Plasma Blob Dynamics. *Physical Review Letters*, 108(21):215002, May 2012.

[3] A. Y. Aydemir. Convective transport in the scrape-off layer of tokamaks. *Physics of Plasmas*, 12(6):062503, 2005.

[4] O G Bakunin. Correlation effects and turbulent diffusion scalings. *Reports on Progress in Physics*, 67(6):965–1032, June 2004.

[5] R Barni and C Riccardi. Advection of long lived density blobs in the turbulent state of a simple magnetized torus plasma. *Plasma Physics and Controlled Fusion*, 51(8):085010, 2009.

[6] Paul M. Bellan. *Fundamentals of Plasma Physics*. Cambridge University Press, 1 edition, 9 2008.

[7] S. Benkadda, T. Dudok de Wit, A. Verga, A. Sen, ASDEX team, and X. Garbet. Characterization of coherent structures in tokamak edge turbulence. *Phys. Rev. Lett.*, 73(25):3403–3406, Dec 1994.

[8] H. L. Berk and G. V. Stupakov. Stability of the gas dynamic trap. *Physics of Fluids B: Plasma Physics*, 3(2):440, 1991.

[9] N. Bian, S. Benkadda, J.-V. Paulsen, and O. E. Garcia. Blobs and front propagation in the scrape-off layer of magnetic confinement devices. *Physics of Plasmas*, 10(3):671, 2003.

[10] J. A. Boedo, D. Rudakov, R. Moyer, S. Krasheninnikov, D. Whyte, G. McKee, G. Tynan, M. Schaffer, P. Stangeby, P. West, S. Allen, T. Evans, R. Fonck, E. Hollmann, A. Leonard, A. Mahdavi, G. Porter, M. Tillack, and G. Antar. Transport by intermittent convection in the boundary of the diii-d tokamak. *Physics of Plasmas*, 8(11):4826–4833, 2001.

[11] S. I. Braginskii. Transport Processes in a Plasma. *Reviews of Plasma Physics*, 1:205, 1965.

[12] J Candy and RE Waltz. An eulerian gyrokinetic-maxwell solver. *Journal of Computational Physics*, 186(2):545–581, 2003.

[13] B. A Carreras, V. E Lynch, D. Del-Castillo-Negrete, B. A Carreras, and V. E Lynch. Nondiffusive Transport in Plasma Turbulence : A Fractional Diffusion Approach. *Physical Review Letters*, 065003(February):1–4, February 2005.

[14] L. Chacón. An optimal, parallel, fully implicit Newton–Krylov solver for three-dimensional viscoresistive magnetohydrodynamics. *Physics of Plasmas*, 15(5):056103, 2008.

[15] S. Cohen and C. Hindmarsh. Cvode, A Stiff/nonstiff Ode Solver In C. *Computers in Physics*, 10(2):138–143, March 1996.

[16] P. Devynck, X. Garbet, Ph. Ghendrih, J. Gunn, C. Honore, B. Pégourié, G. Antar, A. Azeroual, P. Beyer, C. Boucher, V. Budaev, H. Capes, F. Gervais, P. Hennequin, T. Loarer, A. Quémeneur, A. Truc, and J.C. Vallet. Edge turbulence during ergodic divertor operation in tore supra. *Nuclear Fusion*, 42(6):697, 2002.

[17] D. A. D'Ippolito, J. R. Myra, S. I. Krasheninnikov, G. Q. Yu, and A. Yu Pigarov. Blob Transport in the Tokamak Scrape-off-Layer. *Contrib. Plasma Phys.*, 44:205–216, 2004.

[18] D. A. D'Ippolito, J. R. Myra, and S. J. Zweben. Convective transport by intermittent blob-filaments: Comparison of theory and experiment. *Physics of Plasmas*, 18(6):060501, 2011.

[19] W. Dorland, M. Kotschenreuther, and B. N. Rogers. Electromagnetic Gyrokinetic Turbulence Simulations. In *APS Meeting Abstracts*, page 1012P, October 2000.

[20] J. F. Drake and Thomas M. Antonsen. Nonlinear reduced fluid equations for toroidal plasmas. *Physics of Fluids*, 27(4):898, 1984.

[21] J F Drake and B Rogers. ł Nonlinear reduced Braginskii equations with ion thermal dynamics in toroidal plasma. *Physics of Plasmas*, 4(June), 1997.

[22] B Dudson. BOUT ++ Users Manual. *Options*, pages 1–11, 2007.

[23] B D Dudson, M V Umansky, X Q Xu, P B Snyder, and H R Wilson. BOUT ++ : A framework for parallel plasma fluid simulations. *Computer Physics Communications*, 180(9):1467–1480, 2009.

[24] Ben Dudson, Sean Farley, and Lois Curfman. Improved Nonlinear Solvers in BOUT++. pages 1–14, 2012.

[25] T. Evans, R. Moyer, P. Thomas, J. Watkins, T. Osborne, J. Boedo, E. Doyle, M. Fenstermacher, K. Finken, R. Groebner, M. Groth, J. Harris, R. La Haye, C. Lasnier, S. Masuzaki, N. Ohyabu, D. Pretty, T. Rhodes, H. Reimerdes, D. Rudakov, M. Schaffer, G. Wang, and L. Zeng. Suppression of Large Edge-Localized Modes in High-Confinement DIII-D Plasmas with a Stochastic Magnetic Boundary. *Physical Review Letters*, 92(23):235003, June 2004.

[26] Richard Fitzpatrick. *Plasma Physics: An Introduction*. CRC Press, 8 2014.

[27] R. K. Galloway, P. Helander, and a. L. MacKinnon. Cross-field diffusion of electrons in tangled magnetic fields and implications for coronal fine structure. *The Astrophysical Journal*, 646(1):615–624, July 2006.

[28] O. E. GARCIA. Blob transport in the plasma edge: a review. *Plasma and Fusion Research*, 4:019–019, 2009.

[29] O. E. Garcia. Stochastic modeling of intermittent scrape-off layer plasma fluctuations. *Phys. Rev. Lett.*, 108:265001, Jun 2012.

[30] O. E. Garcia, N. H. Bian, and W. Fundamenski. Radial interchange motions of plasma filaments. *Physics of Plasmas*, 13(8):082309, 2006.

[31] O. E. Garcia, V. Naulin, A. H. Nielsen, and J. Juul Rasmussen. Computations of intermittent transport in scrape-off layer plasmas. *Phys. Rev. Lett.*, 92(16):165003, Apr 2004.

[32] Kenneth W Gentle and Huang He. Texas Helimak Texas Helimak device. *Science*, 10(3), 2008.

[33] Ph Ghendrih, A Grosman, and H Capes. Theoretical and experimental investigations of stochastic boundaries in tokamaks. *Plasma Physics and Controlled Fusion*, 38(10):1653–1724, 1996.

[34] Ammar Hakim, Greg Hammet, and Eric Shi. High-order discontinuous galerkin solver for (drift/gyro) kinetic simulations of edge plasmas. APS-DPP 2013, November 2013.

[35] R. D. Hazeltine and J. D. Meiss. *Plasma Confinement*. 1992.

[36] Richard D. Hazeltine and Francois L. Waelbroeck. *The Framework Of Plasma Physics (Frontiers in Physics)*. Westview Press, 1 2004.

[37] Per Helander and Dieter J. Sigmar. *Collisional Transport in Magnetized Plasmas (Cambridge Monographs on Plasma Physics)*. Cambridge University Press, 10 2005.

[38] E. D. Held, J. D. Callen, C. C. Hegna, C. R. Sovinec, T. a. Gianakon, and S. E. Kruger. Nonlocal closures for plasma fluid simulations. *Physics of Plasmas*, 11(5):2419, 2004.

[39] T. C. Hender, R. Fitzpatrick, A. W. Morris, P. G. Carolan, R. D. Durst, T. Edlington, J. Ferreira, S. J. Fielding, P. S. Haynes, J. Hugill, I. J. Jenkins, R.. J. La Haye, B. J. Parham, D. C. Robinson, T. N. Todd, M. Valovic, and G. Vayakis. Effect of resonant magnetic perturbations on COMPASS-C tokamak discharges. *Nucl. Fusion*, 32:2091, 1992.

[40] Takeshi Hirai, Koichiro Ezato, and Patrick Majerus. OVERVIEW ITER Relevant High Heat Flux Testing on Plasma Facing Surfaces. 46(3), 2005.

[41] Wendell Horton. *Turbulent Transport in Magnetized Plasmas*. World Scientific Publishing Company, 10 2012.

[42] M. Kotschenreuther, T. Rognlien, and P. Valanju. Implications of convective scrape-off layer transport for fusion reactors with solid and liquid walls. *Fusion Engineering and Design*, 72(1â"3):169 – 180, 2004. ¡ce:title¿Special Issue on Innovative High-Power Density Concepts for Fusion Plasma Chambers¡/ce:title¿.

[43] S. I. KRASHENINNIKOV, D. A. D'IPPOLITO, and J. R. MYRA. Recent theoretical progress in understanding coherent structures in edge and sol turbulence. *Journal of Plasma Physics*, 74(05):679–717, 2008.

[44] S.I. Krasheninnikov. On scrape off layer plasma transport. *Physics Letters A*, 283(5-6):368–370, May 2001.

[45] B Labit, A Diallo, A Fasoli, I Furno, D Iraji, S H Müller, G Plyushchev, M Podestà, F M Poli, P Ricci, C Theiler, and J Horaček. Statistical properties of electrostatic turbulence in toroidal magnetized plasmas. *Plasma Physics and Controlled Fusion*, 49(12B):B281–B290, December 2007.

[46] B. LaBombard, R. L. Boivin, M. Greenwald, J. Hughes, B. Lipschultz, D. Mossessian, C. S. Pitcher, J. L. Terry, and S. J. Zweben Alcator Group. Particle transport in the scrape-off layer and its relationship to discharge density limit in alcator c-mod. *Physics of Plasmas*, 8(5):2107–2117, 2001.

[47] B. Li, B. N. Rogers, P. Ricci, and K. W. Gentle. Plasma transport and turbulence in the Helimak: Simulation and experiment. *Physics of Plasmas*, 16(8):082510, 2009.

[48] R.J. Maqueda, D.P. Stotler, and the NSTX Team. Intermittent divertor filaments in the national spherical torus experiment and their relation to midplane blobs. *Nuclear Fusion*, 50(7):075002, 2010.

[49] S. McCool, J. Y. Chen, A. J. Wooton, et al. The effect of magnetic perturbations on edge transport in TEXT. *J. Nucl. Mater.*, 176-177:716–720, Dec 1990.

[50] G.R. McKee, C.C. Petty, R.E. Waltz, C. Fenzi, R.J. Fonck, J.E. Kinsey, T.C. Luce, K.H. Burrell, D.R. Baker, E.J. Doyle, X. Garbet, R.A. Moyer, C.L. Rettig, T.L. Rhodes, D.W. Ross, G.M. Staebler, R. Sydora, and M.R. Wade. Non-dimensional scaling of turbulence characteristics and turbulent diffusivity. *Nuclear Fusion*, 41(9):1235, 2001.

[51] Mario Merola, D. Loesser, A. Martin, P. Chappuis, R. Mitteau, V. Komarov, R.a. Pitts, S. Gicquel, V. Barabash, L. Giancarli, J. Palmer, M. Nakahira, A. Loarte, D. Campbell, R. Eaton, A. Kukushkin, M. Sugihara, F. Zhang, C.S. Kim, R. Raffray, L. Ferrand, D. Yao, S. Sadakov, A. Furmanek, V. Rozov, T. Hirai, F. Escourbiac, T. Jokinen, B. Calcagno, and S. Mori. ITER plasma-facing components. *Fusion Engineering and Design*, 85(10-12):2312–2322, December 2010.

[52] D. Meyerson, C. Michoski, F. Waelbroeck, and W. Horton. Effect of chaos on plasma filament dynamics and turbulence in the scrape-off layer. *Physics of Plasmas*, 21(7):072310, July 2014.

[53] C. Michoski, C. Dawson, E. J. Kubatko, J. J. Westerink, D. Wirasaet, and C. Mirabito. Adaptive hierarchic transformations for dynamically p-enriched slope-limiting over discontinuous galerkin systems of generalized equations. *Journal of Computational Physics*, 34:8028–8056, December 2011.

[54] C. Michoski, D. Meyerson, T. Isaac, and F. Waelbroeck. Discontinuous galerkin methods for plasma physics in the scrape-off layer of tokamaks. *Journal of Computational Physics*, to be published.

[55] P. J. Morrison. Magnetic field lines, Hamiltonian dynamics, and nontwist systems. *Physics of Plasmas*, 7(6):2279, 2000.

[56] J. R. Myra, D. A. D'ippolito, S. I. Krasheninnikov, and G. O. Yu. Convective transport in the scrape-off-layer by nonthermalized spinning blobs. *Physics of Plasmas*, 11(9):4267 – 4274, 2004.

[57] J. R. Myra, D. A. Russell, and D. A. D'Ippolito. Transport of perpendicular edge momentum by drift-interchange turbulence and blobs. *Physics of Plasmas*, 15(3):032304, 2008.

[58] Jean C. Perez, W. Horton, K. Gentle, W. L. Rowan, K. Lee, and Russell B. Dahlburg. Drift wave instability in the Helimak experiment. *Physics of Plasmas*, 13(3):032101, 2006.

[59] C. C. Petty. Sizing up plasmas using dimensionless parameters. *Physics of Plasmas*, 15(8):080501, 2008.

[60] W. W. Pfeiffer, R. H. Davidson, R. L. Miller, and R. E. Waltz. ONETWO: A computer code for modeling plasma transport in Tokamaks. Technical report, December 1980.

[61] J. S. E. Portela, I. L. Caldas, R. L. Viana, and P. J. Morrison. Diffusive Transport Through a Nontwist Barrier in Tokamaks. *International Journal of Bifurcation and Chaos*, 17(05):1589–1598, May 2007.

[62] J. S.E. Portela, I. L. Caldas, and R. L. Viana. Tokamak magnetic field lines described by simple maps. *The European Physical Journal Special Topics*, 165(1):195–210, December 2008.

[63] Jefferson S E Portela, E Iber, Instituto De F, Ricardo L Viana, Universidad Rey, and Juan Carlos. FRACTAL AND WADA EXIT BASIN BOUNDARIES IN TOKAMAKS. *Int. J. Bifurcation Chaos*, 17(11):4067–4079, 2007.

[64] D. Reiser. Impact of large island perturbations on turbulent blob transport in tokamaks. *Physics of Plasmas*, 14(8):082314, 2007.

[65] Marshall N Rosenbluth and Albert Simon. Finite larmor radius equations with nonuniform electric fields and velocities. *Physics of Fluids*, 8:1300, 1965.

[66] M.N. Rosenbluth, R.Z. Sagdeev, J.B. Taylor, and G.M. Zaslavski. Destruction of magnetic surfaces by magnetic field irregularities. *Nuclear Fusion*, 6(4):297, 1966.

[67] D. A. Russell, J. R. Myra, and D. A. D'Ippolito. Saturation mechanisms for edge turbulence. *Physics of Plasmas*, 16(12):122304, 2009.

[68] D. D. Ryutov. The dynamics of an isolated plasma filament at the edge of a toroidal device. *Physics of Plasmas*, 13(12):122307, 2006.

[69] Y Sarazin and Ph. Ghendrih. Intermittent particle transport in two-dimensional edge turbulence. *Physics of Plasmas*, 5(12):4214–4228, 1998.

[70] P. B. Snyder, G. W. Hammett, W. Dorland, and I Introduction. Landau fluid models of collisionless magnetohydrodynamics. *Physics of Plasmas*, 4(11):3974, 1997.

[71] T. Tajima, W. Horton, P. J. Morrison, J. Schutkeker, T. Kamimura, K. Mima, and Y. Abe. Instabilities and vortex dynamics in shear flow of magnetized plasmas. *Physics of Fluids B: Plasma Physics*, 3(4):938, 1991.

[72] P Tamain, A Kirk, E Nardon, B Dudson, B Hnat, and the MAST team. Edge turbulence and flows in the presence of resonant magnetic perturbations on mast. *Plasma Physics and Controlled Fusion*, 52(7):075017, 2010.

[73] J L Terry, B Labombard, B Lipschultz, M J Greenwald, J E Rice, and S J Zweben. The Scrape-Off-Layer in Alcator C-Mod Transport , Turbulence , and Flows. (December), 2005.

[74] P W Terry. Suppression of turbulence and transport by sheared flow. 72(1), 2000.

[75] C. Theiler, I. Furno, A. Fasoli, P. Ricci, B. Labit, and D. Iraji. Blob motion and control in simple magnetized plasmas. *Physics of Plasmas*, 18(5):055901, 2011.

[76] C. Theiler, I. Furno, P. Ricci, A. Fasoli, B. Labit, S. H. Müller, and G. Plyushchev. Cross-field motion of plasma blobs in an open magnetic field line configuration. *Phys. Rev. Lett.*, 103:065001, Aug 2009.

[77] K. Ullmann and I. L. Caldas. A symplectic mapping for the ergodic magnetic limiter and its dynamical analysis. *Chaos Solitons and Fractals*, 11:2129–2140, 2000.

[78] M V Umansky, X Q Xu, B Dudson, and L L Lodestro. BOUT Code Manual. *Science*, 2006.

[79] M.V. Umansky, X.Q. Xu, B. Dudson, L.L. LoDestro, and J.R. Myra. Status and verification of edge plasma turbulence code BOUT. *Computer Physics Communications*, 180(6):887–903, June 2009.

[80] J.G. Watkins, T.E. Evans, C.J. Lasnier, R.a. Moyer, and D.L. Rudakov. Target plate conditions during stochastic boundary operation on DIII-D. *Journal of Nuclear Materials*, 363-365:708–712, June 2007.

[81] John Wesson. *Tokamaks*. Clarendon Press Oxford University Press, Oxford New York, 1997.

[82] A.J. Wootton, BA Carreras, H. Matsumoto, K. McGuire, WA Peebles, C.P. Ritz, PW Terry, and SJ Zweben. Fluctuations and anomalous transport in tokamaks. *Physics of Fluids B: Plasma Physics*, 2(2):2879, 1990.

[83] G.S. Xu, V. Naulin, W. Fundamenski, C. Hidalgo, J.A. Alonso, C. Silva, B. Gonçalves, A.H. Nielsen, J. Juul Rasmussen, S.I. Krasheninnikov, B.N. Wan, M. Stamp, and JET EFDA Contributors. Blob/hole formation and zonal-flow generation in the edge plasma of the jet tokamak. *Nuclear Fusion*, 49(9):092002, 2009.

[84] XQ Xu, WM Nevins, and RH Cohen. Dynamical simulations of boundary plasma turbulence in divertor geometry. *New Journal of . . .*, 53:0–15, 2002.

[85] Y. Xu, R.R. Weynants, M. Van Schoor, M. Vergote, S. Jachmich, M.W. Jakubowski, M. Mitri, O. Schmitz, B. Unterberg, P. Beyer, D. Reiser, K.H. Finken, M. Lehnen, and the TEXTOR Team. Reduction of the turbulent blob transport in the scrape-off layer by a resonant magnetic perturbation in textor. *Nuclear Fusion*, 49(3):035005, 2009.

[86] M. Yagi and W. Horton. Reduced Braginskii equations. *Physics of Plasmas*, 1(7):2135, 1994.

[87] N. Yan, A. H. Nielsen, G. S. Xu, V. Naulin, J. Rasmussen, and J. Madsen. Measurement and simulation of intermittent characteristicsin the boundary plasma of east tokamak. *40th EPS Conference on Plasma Physics*, 37D:8028–8056, july 2013.

[88] G. Q. Yu and S. I. Krasheninnikov. Dynamics of blobs in scrape-off-layer/shadow regions of tokamaks and linear devices. *Physics of Plasmas*, 10(11):4413, 2003.

[89] G. Q. Yu, S. I. Krasheninnikov, and P. N. Guzdar. Two-dimensional modelling of blob dynamics in tokamak edge plasmas. *Physics of Plasmas*, 13(4):042508, 2006.

Vita

Dmitry Meyerson was born in Moscow, Russia. He received the Bachelor of Arts degree in Physics from Cornell University in December of 2005. He applied to the University of Texas at Austin for enrollment in their physics program. He was accepted and started graduate studies in August, 2006.

Permanent address: dmitry.meyerson@gmail.com

This dissertation was typeset with LaTeX[†] by the author.

[†]LaTeX is a document preparation system developed by Leslie Lamport as a special version of Donald Knuth's TeX Program.